BIOCHEMISTRY
including biophysical chemistry & molecular biology

Current Topic

pubs.acs.org/biochemistry

Nanostructures of Designed Geometry and Functionality Enable Regulation of Cellular Signaling Processes

Jie-Ren Li,[†] Lifang Shi,[†] Zhao Deng,[†] Su Hao Lo,[‡] and Gang-yu Liu*[,†]

[†]Department of Chemistry, University of California Davis, Davis, California 95616, United States

[‡]Department of Biochemistry and Molecular Medicine, Center for Tissue Regeneration and Repair, University of California Davis Medical Center, Sacramento, California 95817, United States

ABSTRACT: Extracellular matrices (ECM) triggered cellular signaling processes often begin with the clustering of the cellular receptors such as integrin and FcεRI. The sizes of these initial protein complexes or clusters are tens to 100 nm in dimension; therefore, engineered nanostructures could provide effective mimics of ECM for investigation and control of the initial and downstream specific signaling processes. This current topic discusses recent advances in nanotechnology in the context of design and production of matching chemical functionality and geometry for control of specific cellular signaling processes. Two investigations are reported to demonstrate this concept: (a) how the presentation of antigen at the nanometer scale would influence the aggregation of FcεRI, which would impact the formation of activation complexes, leading to the rearrangement of actin in cytoskeleton and degranulation or activation of mast cells; (b) how the engineered nanostructure could guide the initial integrin clustering, which would impact the formation of focal adhesion and downstream cell signaling cascades, leading to polarization, migration, and morphological changes. Complementary to engineered ECMs using synthetic ligands or peptides, or topographic control at the micrometer scale, nanostructures of designed geometry and chemical functionality provide new and effective biochemical cues for regulation of cellular signaling processes and downstream behaviors.

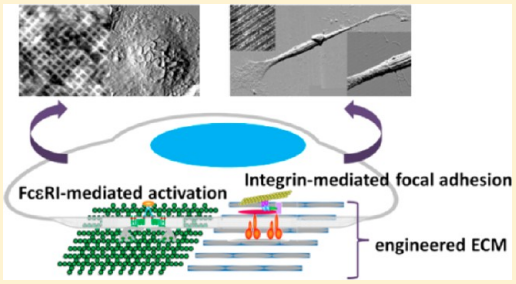

Many cellular signaling processes begin with binding of extracellular signaling molecules and receptors inlaid in the cellular membrane, stimulating a series of events inside the cell, that is, signal transduction processes.[1−5] Well-known signal transduction processes include extracellular matrix (ECM) guided cellular adhesion and spreading,[6−10] migration,[11−13] and proliferation.[10,14,15] Most of these initial bindings are polyvalent in nature, forming complex ligand−protein structures.[16−18] Using an engineered method to mimic ECM materials has, therefore, attracted much attention to regulation or control of specific signaling processes.[19−22] Much progress has been made in the area of topography, typically micrometers in scale, guided cellular behaviors and functions. This topic has been discussed in several comprehensive reviews.[23−26] Synthetic polyvalent ligands represent another approach to mimicking signaling molecules and are also discussed in depth in recent reviews.[16,27−29] Because of the small size, several to 100 nm, of these initial signaling clusters, we and other researchers have been investigating the enabling aspects of engineered nanostructures to study, regulate, and even control the initial and downstream cellular signaling processes.[30−32] Engineered ligand structures or assemblies with nanometer or molecular precision could provide new insight into geometry dependence of signaling pathways.[30,33]

The needs for nanotechnology are illustrated in Figure 1, using two known cellular signaling processes: antigen-mediated mast cell activation[34−37] and integrin-mediated adhesion and spreading of fibroblasts.[13,38−40] In the case of hypersensitivity reaction or mast cell activation, a naturally occurring activation is typically initiated by cross-linking of the receptor-bound, antigen-specific immunoglobulin E (IgE) through a multivalent antigen.[41−44] The cross-linking of FcεRI receptors triggers phosphorylation of cytoplasmic immuno-receptor tyrosine-based activation motif (ITAM) by Src family kinase, Lyn, causing recruitment and activation of other kinases and substrates.[37,43,45] After a series of downstream signaling cascades, this process eventually leads to histamine release through degranulation, which is the well-known outcome of mast cell activation.[41−44] Using synthetic ligands, important insights have been revealed regarding the structural requirements of initial dimers and clusters of IgE−FcεRI complexes.[42,44,46,47] The separation among the nearest neighbor receptors in the activation dimers and clusters is 20 nm, regardless of the history and approaches of cross-linking. Therefore, engineered arrays of nanostructures of antigens on surfaces should provide a new and effective alternative for the polyvalent antigens to guide the cross-linking. Figure 1 shows one example of optimal nanostructure design, that is, two-dimensional (2D) arrays of dots, each containing one antigen. The periodicity of the array is 20 nm to match the spatial requirement of activation dimers. The arrangement of dot

Received: June 7, 2011
Revised: July 11, 2012
Published: July 11, 2012

   dx.doi.org/10.1021/bi200880p | *Biochemistry* 2012, 51, 5876−5893

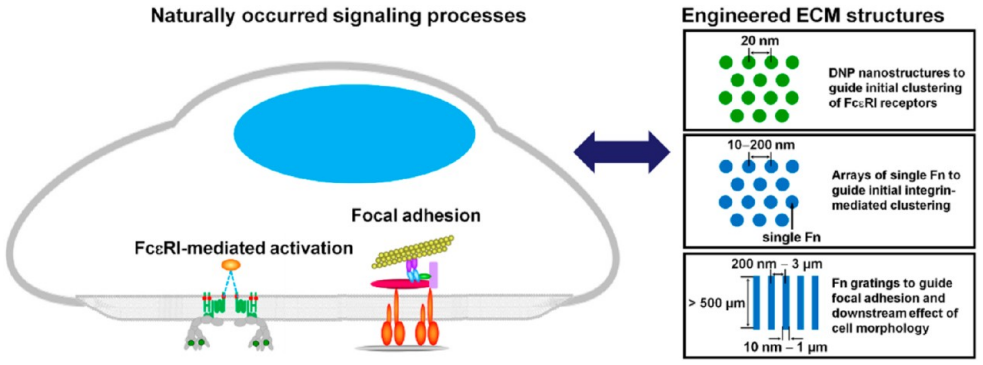

Figure 1. Schematic diagram illustrates the initiation of two cellular signaling processes: integrin clustering and formation of focal adhesion, and FcεRI receptor aggregation and degranulation. On the basis of the knowledge and dimension of these initial clusters, matching designs of nanostructures are shown on the right, as candidates to regulate the clustering and signaling pathways.

arrays follows the 2D closely packed structure, that is, six nearest neighbors for each dot, to optimize the probability of forming clusters from the prospective of geometry.

In the integrin mediated focal adhesion, the integrin at the interface provides a structural link between the ECM outside and the intracellular cytoskeleton, enabling communication between cells and the microenvironment outside.[13,38−40,48] Each integrin consists of two noncovalently bound transmembrane glycoprotein subunits: one α and one β. Each α/β heterodimer has its own ligand-binding specificity and signaling properties that are cell-type specific. The first step in integrin signaling begins with clustering.[48−51] The clustering of the heterodimers is initiated by the binding of ligands, typified by fibronectin which contains the RGD and synergy regions.[52,53] Clustering induces the translocation of molecules including signaling adapters (tensin, p130Cas, paxillin); structural proteins (talin, vinculin); protein kinases (Fak, Src); and actin filaments, while simultaneously enhancing tyrosine phosphorylation at the sites, and finally assembling mature focal adhesions. This initial binding with cytoskeletal and signaling proteins promotes the assembly of actin filaments and stabilizes clusters, which in turn recruits more integrins and enhances ECM binding.[49−51] As a result, the cytoskeletal proteins assemble into focal adhesions, acting as scaffolds for the recruitment of a variety of signaling proteins that control actin remodeling, cell shape, polarity, and movement, and that activate signaling pathways to control survival, proliferation, and differentiation. ***Clustering represents an important and initial step in integrin-ECM mediated cell signaling and function. The sizes of these initial protein complexes or clusters are tens to 100 nm in dimension.*** Following the analogous rational of the previous design, arrays of dots or nanolines with lateral dimensions of tens to 100 nm could provide effective guidance for the alignment of focal adhesion complexes, as shown in Figure 1.

Many other cellular signaling processes also begin by forming clusters at the nanometer scale, such as immunological synapses.[54−58] The earliest step in synapse formation can be directly correlated with topologically driven receptor segregation based on the size of the different receptor−ligand pairs,[59−61] leading to multiple complexes at the cellular contact junction in a concentric circular arrangement, with diameters ranging from tens to hundreds of nanometers.[60,61] One could deduce that a design of concentric circles with the corresponding ligands implicated at the synapse function would be an effective match in terms of geometry. Fully understand that actual biological processes are much more complex than simple geometrical considerations; modification of the designs discussed is anticipated for specific signaling processes. This article explores how effective engineered nanostructures could be in guiding cellular signaling processes, by considering both biochemical functionality and geometrical matching.

Advances in Lithography and Imaging Technologies Enable Construction of Nanostructures with Designed Geometry and Functionality. To produce the nanostructures for guiding specific cellular signaling processes, such as designs shown in Figure 1 and in the discussions in the previous section, two technological challenges must be overcome: (a) nanometer and molecular spatial precision; (b) designated biofunctionalities and activity retainment. Among many approaches tested, soft lithography such as microcontact printing,[62−66] particle lithography,[67−71] and scanning probe based lithography[72−77] could, in principle, meet the technical specifications. Lithographic approaches using atomic force microscopy (AFM) such as nanoshaving,[78−81] nanografting,[82−90] Dip-Pen nanolithography,[91−94] bias-induced lithography,[95,96] and constructive nanolithography[97−100] enable complex geometry production with nanometer precision. Using AFM-based nanolithography in conjunction with microfabrication, complex architectures at multidimensions, from nanometers to hundreds of micrometers may be produced, which match the size of cells and intracellular structures. Figure 2A illustrates the concept of nanografting, that is, combining AFM lithography with the surface chemistry of alkanethiol adsorption on gold surfaces.[72,90] Nanografting is accomplished by force-induced displacement of molecules of self-assembled monolayers (SAMs) matrices, followed immediately by the self-assembly of alkanethiol molecules from solution. The feedback loop used to control the tip position and displacement enables exquisite control of forces applied to the surface, ranging from pN to μN. The procedure of nanografting is relatively simple, starting from imaging (under a small force) alkanethiol SAMs in a liquid medium containing a different kind of thiol, such as dinitrophenyl (DNP) terminated-thiol. As a higher force is applied during the scanning, the matrix thiol molecules are removed by the tip and transported into the solvent. DNP-thiol molecules contained in the solution immediately adsorb onto the freshly exposed gold area following the scanning track of the AFM tip to form designed nanostructures. After completion of designed nanostructures, the products can then be characterized in situ by the same probe at a reduced force.

dx.doi.org/10.1021/bi200880p | *Biochemistry* 2012, 51, 5876−5893

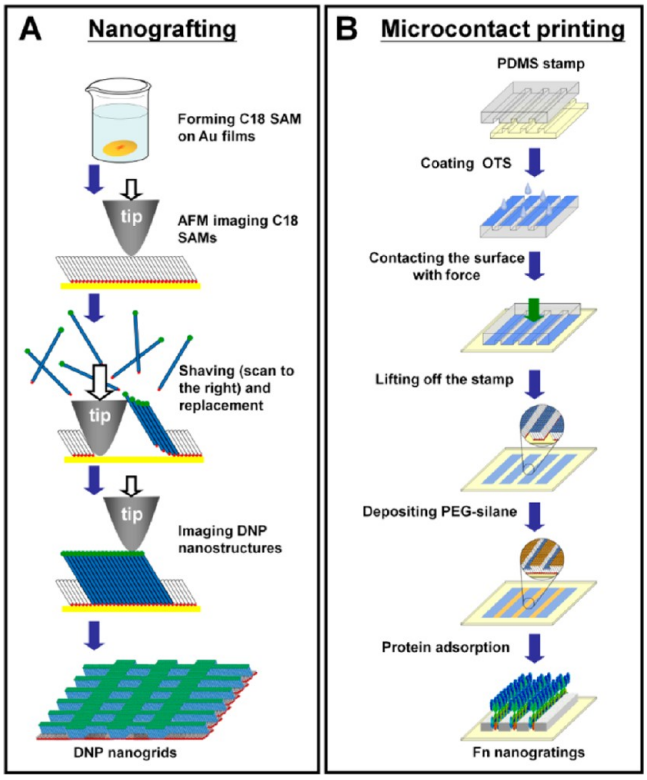

Figure 2. Two methods for production of nanostructures: Lithographic approaches used to fabricate nano- and sub-micrometer structures for regulation of signaling processes. (A) Nanogrids and other nanostructures of antigen could be fabricated using AFM-based nanografting and the surface chemistry of self-assembly: for example, DNP-thiol inlaid in octadecanethiol SAMs; (B) nanolines of Fn may be produced using microcontact printing, and preferential immobilization of Fn on edges of lines.

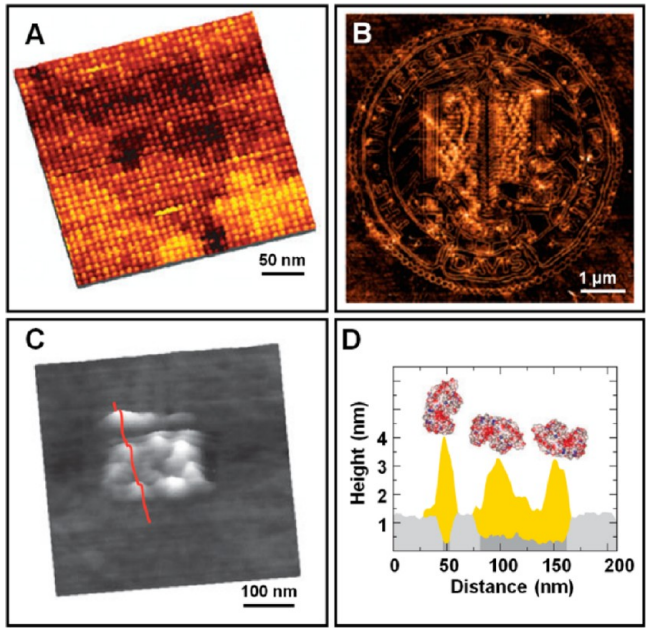

Figure 3. Nanografting enables high-throughput fabrication of complex nanostructures and molecule-resolved imaging to reveal the molecular arrangements on surfaces. (A) An example of a 33 × 33 array of biotin-terminated thiols with a size of 5.2 × 5.2 nm^2 produced by nanografting. (B) The AFM image of the University of California at Davis' seal fabricated by nanografting an aldehyde-terminated thiol into decanethiol SAMs. (C) Lysozyme molecules immobilized onto a nanografted pattern of carboxylate-terminated SAMs. (D) The immobilized lysozyme molecules exhibit different heights and various orientations. Reprinted from ref 90 with permission. Copyright 2008 Annual Reviews.

Nanografting represents the highest precision approach among AFM-based lithography. Figure 3A shows an example in which a 33 × 33 array of biotin-terminated thiols was produced on gold. Each element has a size of 5.2 × 5.2 nm^2 with great uniformity. The smallest nanostructure produced using nanografting is 2 nm × 4 nm, containing only 32 thiol molecules.[90] The capability and practical throughput of nanografting is demonstrated Figure 3B, where the University of California at Davis' seal, 8 × 8 μm^2 in overall size, has been reproduced, using an aldehyde-terminated thiol inlaid in decanethiol SAMs. The entire process only took 10 min to complete with the finest width of 10 nm.[90] For interactions with cells, protein molecules are often used to interact with receptors inlaid in membrane.[1,4] Figure 3C shows an example in which nanostructures containing lysozyme (LYZ) molecules were produced using electrostatic interaction.[90,101] The high selectivity observed at pH 7 results mostly from electrostatic interactions between the LYZ molecules and the carboxylate-terminated nanopatterns produced via nanografting. Three LYZ molecules are positioned along the 10 × 150 nm^2 nanoline, whereas eight protein particles are confined within the 100 × 150 nm^2 nanorectangle. The corresponding combined cursor profiles in Figure 3D reveal that the immobilized protein molecules exhibit two different heights: 4.1 and 3.0 nm. The physical interactions are not specific; therefore, various orientations with respect to the surface are observed for the adsorbed proteins. Because LYZ molecules are ellipsoidal with the approximate dimensions 4.5 × 3.0 × 3.0 nm^3 from X-ray crystallographic studies, the observed heights of 4.1 and 3.0 nm correspond to the side-on and end-on orientations of LYZ, respectively.[90,101]

Soft lithography, such as microcontact printing (μCP), has been widely applied as a promising micropatterning technique due to its simplicity and practical throughput.[62−66] It is widely used in fabricating microstructures, because of its flexibility and its production of designed chemical and topographical features.[102−107] In particular, microcontact printing in conjunction with self-assembly chemistry offers a simple means to introduce designed termini at a designated microgeometry for further electronics, sensor, biochemistry and cellular biology applications. In this study, microcontact printing is used to produce nanolines, utilizing known alkanethiol or organosilane chemistry in conjunction with protein immobilization. A master, typically prepared by conventional photolithography, is used to create a poly(dimethylsiloxane) (PDMS) stamp with micrograting (Figure 2B). The PDMS stamps are easy to use and inexpensive to produce with commercially available templates, thus eliminating the requirement for clean room facilities and expertise. In the printing process, the stamp is coated with the desired ink, such as octadecyltrichlorosilane (OTS), and then pressed against a Si wafer or glass coverslip surface to transfer the ink material. The stamp is lifted off, and the entire surface is exposed to an inert component, such as 2-[methoxy-(polyethyleneoxy)propyl]trichlorosilane (CH_3O-$(C_2H_4O)_{6-9}C_3H_6SiCl_3$, PEG-silane), which would fill the void area left by the stamp ink. To produce nanogratings as required in Figure 1, the micropatterned SAMs are immersed in

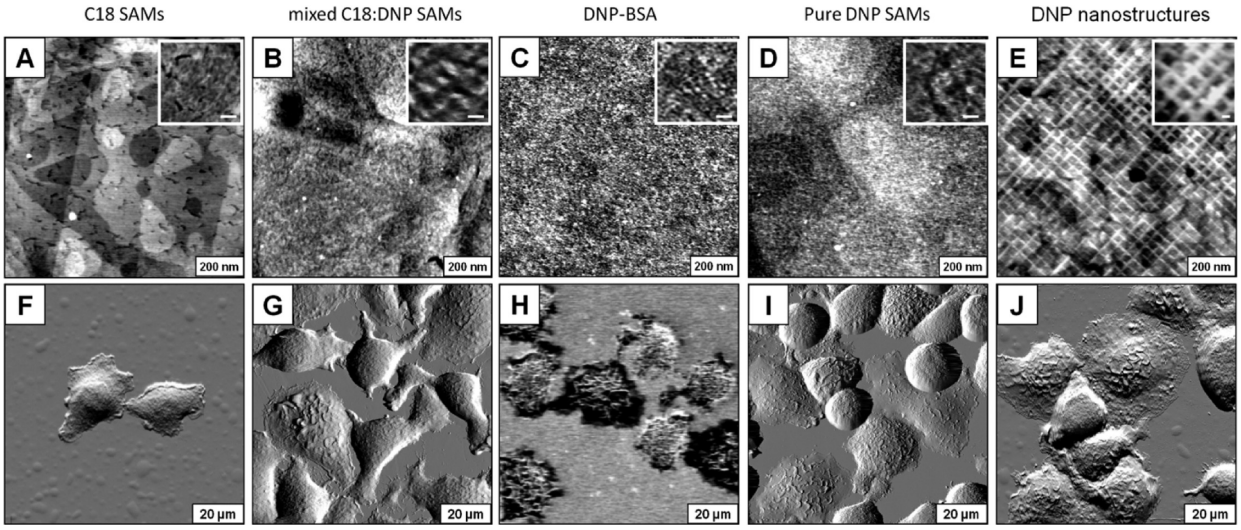

Figure 4. Presentation of antigen in a SAM platform significantly impacts the subsequent behavior of RBL cells. Top row displays a 1 × 1 μm^2 AFM topograph of (A) C18 SAMs prepared by immersing a gold substrate into a solution containing 0.02 mM C18 SAMs in secondary butanol for 24 h, (B) mixed C18 and DNP SAMs prepared by immersing a gold substrate into 0.02 mM mixed C18 and DNP solution with a ratio of 2:1 in a mixture of 5% DMF and second butanol (1:19) for 24 h, (C) DNP-BSA films prepared by soaking a silicon substrate in PBS buffer containing 20 μg/mL DNP-BSA for 1 h, (D) pure DNP SAMs prepared by immersing a gold substrate into 0.02 mM DNP solution in a mixture of *N*,*N*-dimethylformamide and second butanol (1:19) for 24 h, and (E) DNP nanogrids fabricated using nanografting. Each inset is a higher-resolution view of the same surface to reveal active antigen domains at the nanoscale. All images were acquired using contact-mode imaging in defined liquid media. Silicon nitride cantilever with a spring constant 0.1 N/m was used. The imaging force was controlled to be less than 1 nN. The scale bar for each inset image is 20 nm. Bottom row shows the surface of the top row after exposure to anti-DNP IgE-sensitized RBL cells in culture media after 1 h incubation. Images in (F), (G), (I), and (J) were 80 × 80 μm^2 scans, acquired using AFM in PBS buffer. Si cantilever with a spring constant 0.05 N/m was used, and the imaging force was controlled to be less than 1 nN. Mast cells on DNP-BSA films (H) were characterized by SEM. The morphology of activated RBL cells was observed with a Hitachi S-800T FE-SEM with the routine accelerating voltage of 2.5 kV.

fibronectin (Fn) solutions. Polyethylene glycol (PEG) is known to resist protein adsorption and cell adhesion.[108−110] Thus Fn molecules selectively attach to the methyl terminated micro-lines, as illustrated in Figure 2B. As demonstrated later, the Fn molecules exhibit more favored adsorption at the edges of gratings than the bulk, and thus F-rich nanoline (typically with one Fn molecular width) can be produced. The apparent height of Fn domains is designed to be higher than the surrounding areas, providing a sterically favored environment for effective integrin clustering upon binding, which activates focal adhesion and downstream cascades.

ENGINEERED ANTIGEN NANOSTRUCTURES OFFER A UNIQUE MEANS FOR REGULATING ANTIBODY-MEDIATED CELLULAR SIGNALING PROCESSES

Nanostructures of Antigen in Comparison with Previously Reported Presentations. We have produced and characterized the nanostructures of 2,4-dinitrophenylated alkanethiol ($[DNPNH(CH_2)_5COO(C_2H_4O)_4CO(CH_2)_{15}S]_2$, DNP-thiol) in comparison with previously used presentations of antigen, as illustrated in Figure 4 (top row). The DNP-thiol with oligo-ethylene oxide linkers has been used for preparing SAMs used in antigen-based biosensors[111] and in investigations of IgE-FcεRI mediated signaling processes.[32,112] A series of DNP-containing SAMs were characterized at nanometer resolution, including mixed DNP-thiol/C18 = 1:2 SAMs, pure DNP-thiol SAMs, and DNP nanogrids produced using nanografting. These SAM systems will also be compared with 2,4-dinitrophenylated bovine serum albumin (DNP-BSA) layers, in terms of local structure of antigen groups, and activation efficiency. Taking advantage of high AFM resolution, the DNP domain size, separation, and apparent height with respect to surrounding area can be measured in correlation to the activation efficiency.

The C18 SAM serves as a control because of its well-known structure, and no activation of rat basophilic leukemia (RBL) mast cells is expected due to lack of antigen and adhesive forces. Figure 4A reveals a typical 1 × 1 μm^2 AFM image of C18 SAMs on the Au(111) surface, the contrast of which reflects the gold structures underneath such as flat terraces separated by single atomic steps. The lateral dimension of Au(111) terrace ranges from tens to hundreds of nanometers, under thermal evaporation in a vacuum. The zoom-in image inserted in Figure 4A reveals the morphology of this SAM: closely packed C18 domains of several nanometers in lateral dimension, separated by domain boundaries. The apparent height of the C18 domain is 0.15 ± 0.03 nm, that is, a very flat homogeneous surface at the nanometer scale, consistent with previously reported heights.[72,76,77,85,87,90] The C18 SAMs are among the highest coverage and crystallinity among SAMs.

DNP-BSA layers have been widely used as surface bound antigens for investigation of mast cell activation.[113−115] Figure 4C displays the morphology of DNP-BSA films on the silicon surface. The DNP-BSA films were prepared by soaking a silicon substrate in phosphate buffered saline (PBS) buffer containing 20 μg/mL DNP-BSA for 1 h, following previously reported protocols.[116] The immobilization is of physical adsorption in nature, as previously reported.[117−119] The physical interactions are not specific; therefore, various orientations with respect to the surface are observed for the adsorbed proteins. Figure 4C exhibits a typical AFM image (1 × 1 μm^2) of DNP-BSA on Si(111) surface. The image was acquired in a PBS buffer. Protruding domains with bright contrast are evident through-

dx.doi.org/10.1021/bi200880p | *Biochemistry* 2012, 51, 5876−5893

out areas of the surface, indicating that a large amount of DNP-BSA molecules has been adsorbed onto the surface. High-resolution AFM image inserted in Figure 4C reveals that the diameter of DNP-BSA features measures 5.9 ± 3.3 nm. The DNP-BSA were immobilized almost randomly on the silicon surface, with the center-to-center separation from 5.6 to 18.9 nm, the edge-to-edge separation from 3.2 to 11.7 nm, and an apparent height of 0.4 ± 0.3 nm.

DNP SAMs offer a simpler and more stable alternative than DNP- BSA and thus have been used as surface-bound antigens in investigations of degranulation.[112] Figure 4D reveals high coverage DNP SAMs prepared in a mixed solvent of 5% *N*,*N*-dimethylformamide (DMF) in 2-butanol. The Au(111) film topograph underneath is not as clearly resolved as those of the C18 SAM, indicating a heterogeneous layer on surfaces whose roughness is comparable to gold single atomic steps. Zooming-in view shown in the inset reveals that DNP SAMs exhibit lateral heterogeneity: bright features (DNP domains) of near circular shape with a diameter of 6.7 ± 2.9 nm, surrounded by dark regions. The center-to-center separation of nearest neighbor DNP domains ranges from 7.3 to 24.2 nm. The edge-to-edge separation of DNP domains is from 3.9 to 15.8 nm. The bright domain measures 0.5 ± 0.2 nm taller than the surrounding areas, consistent with a structure of more densely packed DNP domains surrounded by lower density/coverage of DNP regions. The more closely packed domains deform less under the AFM load, which manifests into bright contrast in the topographic images.

Mixed SAMs formed by natural growth enable a certain degree of control in local heterogeneity and were used previously as surface bound hepten in the activation of RBL cells.[32,112] Figure 4B exhibits a typical 1 × 1 μm^2 AFM image of mixed C18/DNP SAMs on Au(111) surface. The characteristic structures of gold substrate are not as clearly visible as in C18 SAMs, an indication of heterogeneity at the nanometer scale that is comparable to Au(111) steps. The high-resolution AFM image in Figure 4B inset reveals the segregated DNP domains inlaid in C18 regions, appearing as bright and dark contrast, respectively. This phase segregation behavior is characteristic for binary SAMs.[120,121] The DNP domain size is 9.6 ± 5.8 nm, with the center-to-center separation ranging from 10.7 to 32.5 nm and the edge-to-edge separation from 5.6 to 23.6 nm. The DNP domains are 0.3 ± 0.1 nm taller than the surrounding C18 matrix.

In contrast to previously discussed presentations of surface bound heptens, nanostructures of DNP are produced at a designed geometry, location, and local environment, using nanografting. The AFM image in Figure 4E shows an example of these engineered structures: DNP nanogrids inlaid in C18 SAM.[32] The backbone of the DNP-thiol is longer than that of C18, and thus the DNP nanostructures appear 1.4 ± 0.3 nm taller than the surrounding C18 matrix SAMs. The high-resolution AFM image shown in the inset in Figure 4E indicates that these DNP nanogrids have relatively sharp edges. The lines are 17.1 ± 1.7 nm wide as measured by the full width at half-maximum (fwhm), with the edge-to-edge separation from 22.1 ± 2.3 among the nearest neighbor lines. The periodicity of DNP nanogrids measures 40.4 ± 2.6 nm.[32] ***Compared to naturally grown SAMs containing DNPs, the engineered nanostructures consist of DNP domains with designed geometry (grids), size, and local environment (1.4 nm taller than hydrophobic regions).*** Molecules at the bulk of these domains are more closely packed than naturally grown ones due to the spatial confined self-assembly during nanografting.[82,83,85] The enabling aspects of tuning local structure should be of great importance in guiding subsequent biochemical reactions, such as antibody recognition and cellular behavior.

Cellular Morphology and Behavior Depend Sensitively on the Presentation of Ligands at Nanoscale. Cellular responses to the presentation of DNP functionality upon exposure of the aforementioned surfaces to RBL cells, soaking in 0.5 μg/mL anti-DNP IgE overnight for sensitization in the incubation environment, are shown in Figure 4, bottom row. The selection of 1 h incubation time is to ensure the capture of dramatic morphological changes at the membranes, before the granule regeneration process which could take up to a couple of days.[41−44] The presence of DNP domains greatly enhances the adhesion of RBL; for example, the number of cells on C18 SAM is significantly fewer than the rest. In addition, the spreading and morphology differ: with nanogrids exhibiting the highest level of spreading, followed by pure DNP SAMs, mixed DNP/C18 SAMs and DNP-BSA layers. Mast cells do not seem to spread on C18 SAMs due to the low biocompatibility and lack of antigen on this surface (Figure 4F). On mixed DNP/C18 SAMs (middle left region in Figure 4G), RBLs spread on the surface (interfacial area of 627 μm^2). This level of spreading is similar to that on DNP-BSA films (591 μm^2), and on pure DNP SAMs (758 μm^2), as shown in Figure 4, panels H and I, respectively. Highest level of spreading is found on DNP nanogrids, which measures 1297 μm^2 as shown in Figure 7J. Even though the surface coverage of DNP of nanogrid surface is identical to that of mixed DNP/C18 SAMs, cells exhibit a higher degree of spreading on nanogrids. This observation clearly indicates that the binding between DNP and IgE (at the membrane of RBLs) plays a key role in subsequent cellular motion and signaling. Thus the local structure of DNP domains, not the absolute coverage, impacts the arrangement of IgE binding, cytoskeletal components, leading to variations of locomotion and spreading.

In addition to adhesion and spreading, and more importantly and pertaining to this work, nanoscopic features of cellular membranes also depend on antigen presentation. The membrane morphology and structure are known to reflect the activation status of mast cells.[113−116,122] Previous studies have established that appearance of membrane ridges are one signature of IgE-FcεRI-mediated activation, in contrast to a high density of microvilli, which indicates resting status of RBL cells.[113−116,122−124] Taking advantage of the high-resolution and versatility of imaging under near physiological conditions, the membrane structure is visible and quantifiable in 3D using AFM. The RBL mast cells on C18 SAMs only exhibited microvilli (Figure 4F), consistent with a lack of activation. On mixed DNP/C18 SAMs, both microvilli and membrane ridges were evident (Figure 4G). Three cells exhibit membrane ridges, which is characteristic of IgE−FcεRI-mediated activation. Six other cells are resting, whose membranes exhibit a high density of microvilli. Upon attachment on DNP-BSA surfaces, membrane ridges appeared, as shown in Figure 4H. The bright contrast in the SEM image represents the characteristic membrane ridges that have been reported previously.[113−115] Four cells were activated, while the remaining four are resting. In Figure 4I, RBLs are adherent on the pure DNP SAM with 5 out of 11 cells revealing the characteristic membrane ridges or antibody mediated activation. Membrane ridges are present on most cells on nanogrids of DNP, based on the AFM characterization shown in Figure 4J: 6 out of 9 show very

evident ridges. Taking advantage of the high spatial resolution and accuracy in height measurement, AFM enables imaging of the lateral and vertical dimensions of membrane ridges. The number and the height of ridges were found to represent the degree of activation, from our previous AFM investigation validated by confocal imaging.[116] A fully activated RBL cell seemed to exhibit ridges longer than 3 μm, and ridge height > 0.5 μm taller than the surrounding membrane.[116] RBL cells on nanogrids exhibit the highest degree of activation. Taking the cell located in the upper middle region, 19 ridges are visible on the cortical membrane with the length from 3.3 to 9.7 μm, and the height measures 0.5−0.7 μm. After AFM imaging on hydrated cells, the activation status of RBL was also confirmed using laser scanning confocal microscopy with the cytoskeletal actins labeled by phalloidin assay following previous protocols.[116] In Figure 5, the characteristic membrane ridges in RBL mast cells correspond well with the heterogeneous F-actin network in their cytoskeleton underneath. Upon antibody mediated degranulation or activation, F-actin rearranges from a relatively homogeneous distribution to a heterogeneous network.[116] The combined study not only provides validation that AFM can identify activated cells without using tags or labels, but also provides new insight, for example, into the structural origin of the observed membrane ridges being the result of bilayer membrane decorated over the actin network in the cytoskeleton.[116]

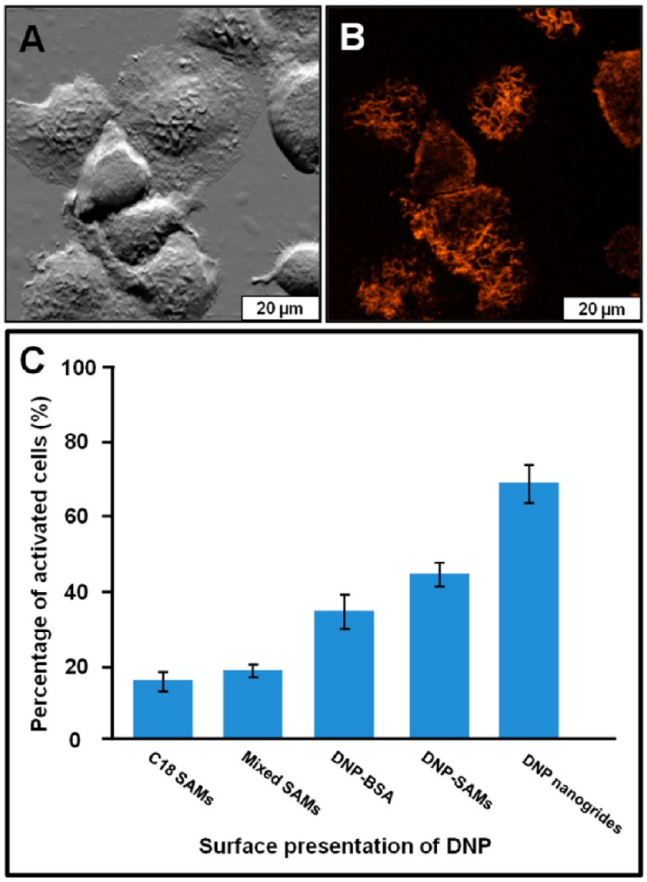

Figure 5. AFM image (A) and corresponding confocal image (B) of RBL mast cells on DNP nanostructures (of Figure 4E). Scale bars: 20 μm. Si cantilever with a spring constant 0.05 N/m was used for AFM characterization, and the imaging force was controlled to be less than 1 nN. Upon completion of AFM imaging, the sample was stained using phalloidin assay, and then imaged under a FV1000 confocal microscope (Olympus America), using excitation of 543 nm and emission between 555 and 630 nm. The confocal image was acquired using a Plan Apo N (60×, N.A. = 1.42) oil immersion bright-field objective with a working distance of 0.15 mm. The 2D project confocal image in B was displayed using Z-projection to present the 3D spatial distribution of characteristic membrane ridges. (C) Activation efficacy, extracted by counting the activated RBL cells, as a function of the surface presentation of DNP antigens.

Since AFM images provide a definitive means to count cells and identify activated population, the efficacy of activation can be quantified and compared among the five presentations discussed previously. Taking DNP nanogrids as an example, there are a total of nine cells in Figure 5A (also in 4J). Among them, six cells exhibit membrane ridges based on the AFM topograph shown in Figure 5A. Subsequent confocal microscopy imagery in Figure 5B confirms the presence and correspondence of the heterogeneous network of F-actin. Therefore, the activation efficiency is quantified as 66.7% (= 6/9). The activation is highly dependent on the presentations of antigen, as shown in Figure 5C, from 18% (C18 SAMs), 21% (mixed DNP/C18 SAMs), 36% (DNP-BSA), 45% (pure DNP SAMs) to 69% (DNP nanostructures). Even though the DNP coverage in nanogrids is only equal to the mixed SAMs, and is much lower than DNP-BSA and pure DNP SAMs, it exhibits higher activation potency than all other presentations of surface bound antigens. This evidence further demonstrates the importance of local structure of DNP domains over other factors such as antigen concentration.

Proposed Mechanism for the Superior Activation Potency by Nanostructures of DNP. To understand the high activation potency of DNP nanostructures, molecular level packing of DNP has been studied using AFM. As shown in Figure 6A, mixed C18/DNP SAMs exhibit phase segregation at the nanometer level, DNP domains appear as bright features, while C18 regions appear darker in AFM topographic images. The cursor profile under image 6A indicates the typical domain size of DNP in this mix is 7.4 nm, with 0.3 nm above the surrounding C18 matrix. The interdomain separation (normally referred to as center-to-center) is 18.7 nm. Pure DNP SAMs also exhibit phase segregation and lateral heterogeneity, as shown in Figure 6B. Typical domains have a lateral dimension of 5.6 ± 1.8 nm, with apparent height of 0.5 nm, as measured by the cursor profile under image 6B. The structural characterization indicates that DNP domains exhibit taller apparent height in the pure DNP SAM than in the mixed C18/DNP SAMs, an observation that is consistent with the molecular packing and deformation under AFM load. The domains are located closer to each other than as with mixed SAMs, as separation measures 10.2 nm. The AFM image in Figure 6C shows that DNP nanogrids consist of arrays of nanosquares with single-line borders. Each line in the nanogrids represents the DNP domains. Unlike SAMs which exhibit variation in DNP domain size, all lines are 17.1 ± 1.7 nm wide and 1.4 nm taller than the surrounding C18 SAMs, as shown in the cursor profile in Figure 6C. The edge-to-edge separation among nearest neighbor lines is 22.1 ± 2.3 nm in both directions. Among the three antigen candidates, the apparent domain height increases from 0.3 nm (mixed DNP/C18 SAMs), to 0.5 nm (pure DNP SAMs) to 1.4 nm (DNP nanogrids). Mixed C18/DNP SAMs and pure DNP SAMs exhibit randomly distributed DNP domains with sizes ranging from 5.6 to 24.2 nm. In contrast, engineered nanogrids contain

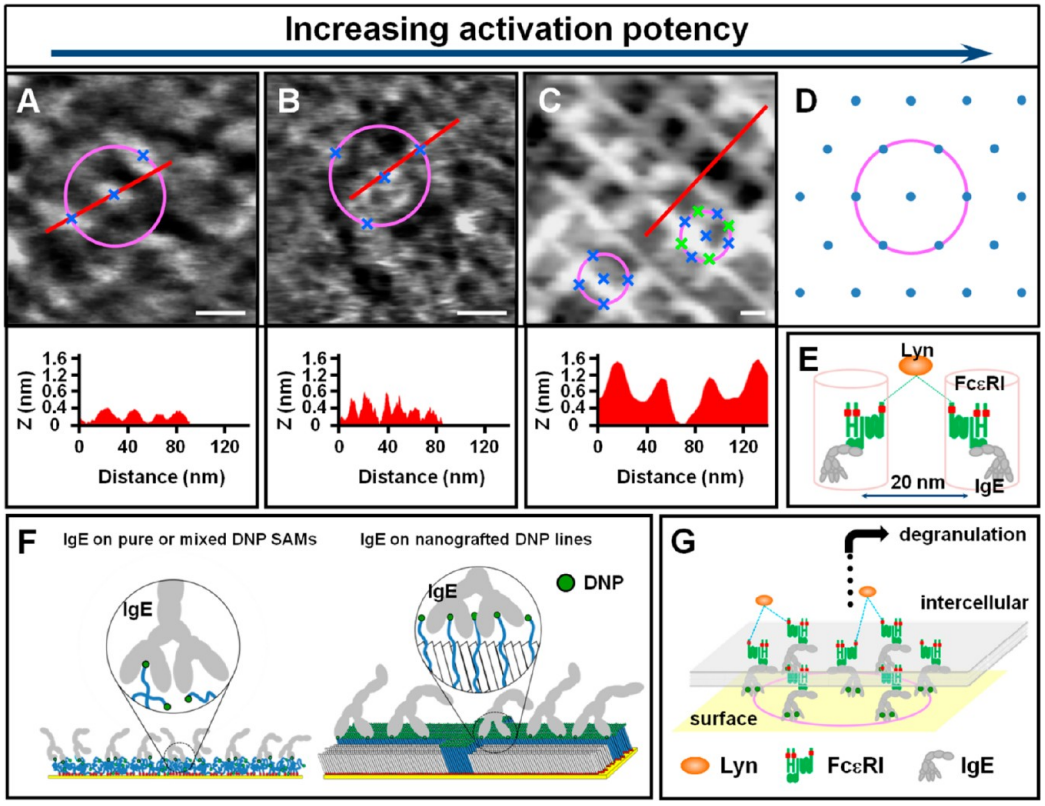

Figure 6. Proposed rationalization for the superior efficacy of DNP nanostructures in activating RBL cells. The high-resolution AFM images reveal the surface morphologies of (A) mixed C18/DNP SAMs, (B) pure DNP SAMs, and (C) DNP nanostructures. The cursor profile under each imaging reveals the local environment of the typical DNP nanodomains, the domain size, and their apparent height above the surrounding. The center of each pink circle is a representative DNP domain, and the radius of the circles is 20 nm, that is, the separation of two adjacent IgE–FcεRI molecules known as an activation dimer shown in (E). Therefore, the blue cross presents the DNP domains which could serve as the binding sites for one IgE–FcεRI complex, in order to form dimers with the central complex. (F) A schematic diagram illustrates the favored binding with IgE by nanogrids of DNP, due to adequate apparent height and sufficient local concentration. (G) A simple model to illustrate the concept that the design in (D) and nanogrids in (C) provide the best match for the formation IgE–FcεRI activation clusters.

arrays of DNP squares with a uniform line width of 17.1 ± 1.7 nm.

The local structure of DNP impacts the subsequent recognition by IgE, assuming IgE molecules are individual antibodies in solution phase above the SAMs. The concept that ligand presentation at the molecular or nanometer level significantly impacts the subsequent biochemical reaction has been realized by researchers during the past two decades.[125−129] It is known that protein binding to ligands at surfaces can be more efficient via long, flexible polymer tethers than via very short ones.[130−132] Such tethers may serve to orient the ligands, which could aid in the efficacy of antibody binding depending on the relative hydrophobicity of the linker. Long, flexible, hydrophilic ethylene oxide linkers have been demonstrated to improve hapten presentation at bilayer interfaces.[133,134] In fact, DNP haptens with sufficiently short or long hydrophobic spacers are known to be less effective for antibody binding than those with intermediate chain lengths.[135,136] As illustrated in Figure 6F (on the left), the molecular level packing in mixed DNP/C18 or pure DNP SAMs resulted in small apparent height, or less exposure of DNP termini. It is thus difficult for DNP termini to probe into the Fab domains and bind to the IgE molecules. For specific and stable antibody–antigen recognition, divalent bindings between the two Fab domains and two matching DNP antigens underneath are preferred, as illustrated in Figure 6F (right). Additionally, the rigidity of the DNP termini should be sufficient to keep them taller than its surrounding, and flexible enough to enter the Fab pocket.[136] DNP domains in the mixed SAMs have sufficient size and flexibility, but the apparent height of 0.3 nm makes it sterically hindered for effective binding with a Fab pocket. Pure DNP SAMs have higher antigen concentration than mixed layers, but the relatively low apparent height of DNP domains 0.5 nm also makes IgE recognition less favorable. In contrast, nanografted DNP SAMs form more ordered and close-packed structures of nanoline due to the effect of spatial confinement.[82,83,85] The lines are 1.4 nm taller than C18 SAMs, providing a sterically favored environment for *the DNP termini at the edges* to be recognized by the antibodies. Since nearest neighbor DNP termini are readily available along the line, bivalent recognition (that is, finding two DNP with 20 nm separation) along the nanoline is highly favored. The antibody binding strongly depends on antigen presentation, such as size, flexibility, rigidity, and domain separation of the DNP surfaces. In comparison among the three top candidates, the DNP nanogrids provide the following intrinsic advantages: (a) flexibility and rigidity of DNP domains at the edges; (b) less steric hindrance of taller DNP domains for antibody–antigen recognition; (c) well-defined edge-to-edge separation to match the spatial requirements for the IgE–FcεRI dimer and cluster formation.

dx.doi.org/10.1021/bi200880p | *Biochemistry* 2012, 51, 5876−5893

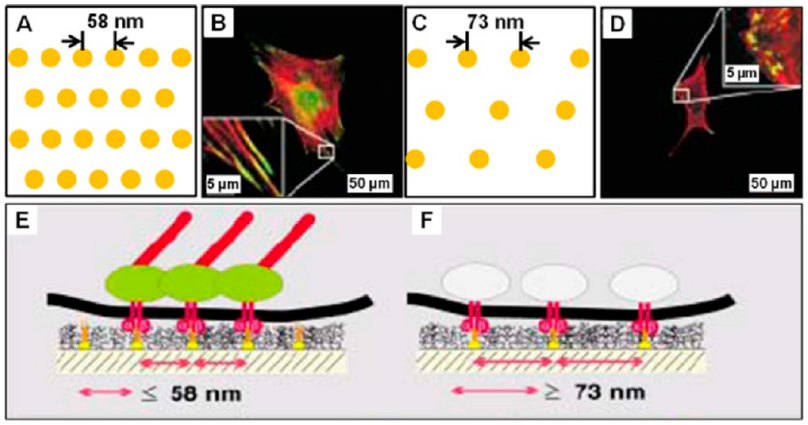

Figure 7. Nanodot arrays of RGD for switching initial integrin clustering. (A) and (C) are schematic diagrams of the designs with the separation of 58 and 73 nm, respectively. (B) and (D) are confocal micrographs of MC3T3-osteoblasts stained for vinculin (green) and actin (red) after 24 h incubation in the nanodot arrays. Zoom-in images are shown as insets. (E) A separation of 58 nm could activate focal adhesion, leading to actin stress fibers and cellular spreading. (F) A separation of 73 nm could not initiate integrin clustering, thus limited the downstream cascades, due to lack of fiber bundles. Reprinted from ref 30 with permission. Copyright 2004 Wiley-VCH.

In the case of our investigations shown in Figures 4 and 5, IgE molecules are exposed at the membrane of RBLs after sensitization protocols.[32,116,123] Since the presentation of DNP impacts the binding with IgE as discussed above, these recognition events lead to variation in activation, as each IgE is linked via binding with a FcεRI receptor at the cellular membrane. As described in the previous section, forming basic activation dimers and clusters fulfills the critical spatial requirement for subsequent protein binding, such as Lyn and Syk, and downstream activation.[42,44,46] The separation between adjacent IgE−FcεRI complexes is suggested to be 20 nm in the dimers and clusters, as illustrated in Figure 6E. Using simple statistical analysis,[32] we can compare the probability to form dimers and clusters by selecting a typical DNP domain first and then draw a circle of 20 nm radius around this typical binding site. If the circle hits another DNP domain, as in the case of the two SAMs, there is likely an adjacent IgE−FcεRI complex, assuming high affinity of IgE and DNP. Among the two SAMs shown in Figure 6A,B, the circles hit two and three DNP sites, respectively, which provide a probability of finding an adjacent complex and of forming activation dimers. In the case of DNP nanogrids in Figure 6C, the two representative binding sites were selected from the middle of the line or at the cross-section, respectively. Following previous exercises among SAMs, the two circles hit four and eight sites, respectively. If one edge is occupied, spatial hindrance (17 nm is less than 20 nm) may hinder the other edge from attracting another IgE−FcεRI complex; thus among eight potential IgE−FcεRI receptor binding sites, we only counted four as viable, as shown in Figure 6C. Even only counting the minimum number, DNP nanostructures still exhibit the statistical advantage in forming activation dimers and clusters over the other presentations. In addition, the DNP sites in nanogrids also exhibit a higher probability of binding IgE due to the higher apparent height. The combined advantages lead to the superior activation efficiency by nanogrids. If this rationale remains valid, we project that the optimal design should be the presentation shown in Figure 6G, where DNP nanodots are arranged in hexagonal arrays with 20 nm periodicity, although we fully recognize that the actual situation could be more complex than offered by simple statistical analysis.

Given the length scale at which signaling clusters are in the range of nanometers, nanofabrication techniques provide an advantage of positioning membrane receptor-binding ligands with nanometer precision for regulation of specific signaling pathways. In the case of DNP nanogrids, the ligand distribution, geometry, and local environment are designed to optimize antibody binding and cluster formation.[32] This finding could be extrapolated into generic practice that nanoengineered structure with well-defined geometry and functionality can serve as a platform to regulate cellular responses to stimuli, and receptor-mediated cell signaling pathways, and downstream cellular behaviors.

NANOSTRUCTURES OF FIBRONECTIN PROVIDE EFFECTIVE BIOCHEMICAL CUES FOR REGULATION OF THE FOCAL ADHESION AND SUBSEQUENT BEHAVIORS OF FIBROBLAST CELLS

Nanodot Arrays of RGD for Initiating Integrin Clustering and Focal Adhesion. As also discussed in earlier sections, integrin clustering along the cell membrane is an important step in integrin-ECM mediated focal adhesion, cell signaling, and function.[53,137−139] In order to achieve the nanoscale positioning of ECM ligand molecules and investigate function behind the molecular arrangement of single integrins in cell adhesion, Spatz and co-workers developed a hexagonally close-packed rigid template of cell-adhesive gold nanodots using block copolymer micelle nanolithography.[30] The diameter of integrin in the cell membrane is between 8 and 12 nm.[140] Therefore, the designed diameter of Au nanodots is 8 nm on a PEG passivated background, in order to provide a single anchor point for only one integrin. Arrays of nanodots containing RGD ligands provide initial binding sites for integrin inlaid in cellular membrane.[30] Since integrin clustering is required for formation of mature focal adhesion, the focal adhesion may be turned "on" or "off" by altering the separation of RGD dots. In fact, the cultured MC3T3-osteoblasts showed remarkable sensitivity to the separation of these RGD dots,[30,33] as shown in Figure 7. As the separation among these gold nanoparticles was increased from 28 to 85 nm, focal adhesion was altered.[30] For example, on a nanopatterned surface with separation of 58 nm (Figure 7A), vinculin clusters (green) and actin stress fibers (red) were observed in confocal images

dx.doi.org/10.1021/bi200880p | Biochemistry 2012, 51, 5876−5893

(Figure 7B), indicating mature focal adhesion. However, a separation of 73 nm is found to be less effective in formation of integrin clusters, in which little vinculin clusters and actin fibers were visible (Figure 7C,D). The rationalization is shown in Figure 7E: a separation of RGD dots by 58 nm or smaller could lead to effective integrin clustering upon binding, which activates focal adhesion and downstream cascades, leading to formation of actin stress fibers. In contrast, the separation of 73 nm could not form integrin clustering upon binding integrins, which hinders the formation and alignment of focal adhesion sites, and thus could not lead to formation of actin stress fibers downstream (Figure 7F). A universal separation threshold of 58−73 nm is proposed for integrin clustering,[33] which is essential for the effective formation of mature focal adhesion and the propagation of integrin mediated signaling processes.[30,33]

NANOGRATINGS OF FIBRONECTIN FOR GUIDING FOCAL ADHESION ALIGNMENT AND CELLULAR MORPHOLOGY

Fabrication and Characterization of Fn Gratings. To guide focal adhesion and the downstream effect of cell morphology, Fn gratings were fabricated via microcontact printing followed by protein immobilization, as illustrated in Figure 2. Solution deposition was applied to generate organosilane gratings for subsequent Fn immobilization via hydrophobic interaction.[141−144] Spatial selectivity is achieved by using hydrophobic lines for protein attachment, surrounded by PEG to resist protein adsorption.[141−145] The surface bound Fn molecules, following this immobilization protocol, should remain bioactive and viable as demonstrated by previous studies.[143,144,146,147]

Fn gratings are shown in Figure 8. The pattern covers the entire 1 × 1 cm^2 surface area, which is sufficient for in vitro investigations.[148] The length of each Fn line is sufficiently continuous across the surface. The printing time used to transfer OTS is less than 1 min. The remaining regions are blocked with a protein resistant 2-[methoxy-(polyethyleneoxy)-propyl]trichlorosilane ($CH_3O(C_2H_4O)_{6-9}C_3H_6SiCl_3$, PEG-silane). Fn lines measured taller than the surrounding PEG regions by 3.2 ± 0.5 nm. The width of Fn lines is 0.89 ± 0.08 μm, with an edge-to-edge separation of 0.65 ± 0.03 μm among nearest neighbor lines. The periodicity of Fn grating is 1.55 ± 0.10 μm (Figure 8C,D). To compare the Fn nanogratings with controls, Fn covered surfaces were prepared via a commonly adopted method, for example, by immersion of a glass coverslip or a silicon wafer in a 10 μg/mL Fn solution in 1× phosphate buffered saline (PBS) for 1 h. The structure at the nanometer scale has been characterized using AFM, and the images are shown in Figure 8A,B. Fn layers in grating regions appear nonhomogenous with more Fn molecules at the edges of the bands. The preferential binding of Fn to edges of hydrophobic domains has been reported previously and was attributed to less steric hindrance.[149] As a result of nonhomogeneous immobilization of Fn, our microcontact printing protocols produced nanolines of Fn, with a separation of 0.89 ± 0.08 μm (width of grating).[148] ***Therefore, we refer to the line arrays as nanogratings of Fn in this case.*** The separation between neighboring Fn is comparable to the protein size, less than 20 nm, and each line is continuous beyond cellular dimensions, which is sufficient to guide linear clustering of integrin along the line. The width of the grating is 0.89 ± 0.08 μm, much larger than the tip of filopodia,[150] and sufficient to accommodate initial attachment.

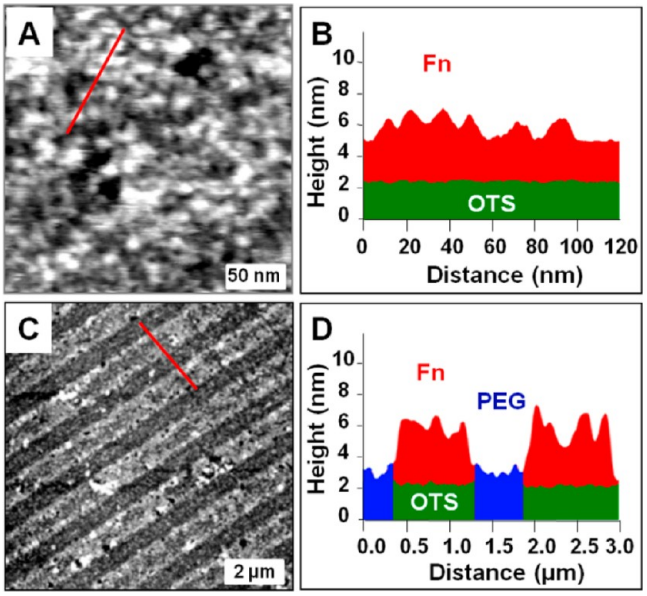

Figure 8. AFM topographic images of (A) control surface prepared by immersion OTS coated silicon wafer in 10 μg/mL Fn solution in PBS, and (C) Fn gratings produced via a method shown in Figure 2B. (B) and (D) are the cursors profiles as indicated in (A) and (C), respectively. Zero height is (D) is referred as the surface of silicon water. AFM images are acquired under tapping mode in PBS solution using MSNL cantilever with a spring constant of 0.1 N/m.

In contrast to Fn grating, an almost full layer of Fn formed when soaking OTS SAMs in 10 μg/mL Fn solution for 1 h. We have systematically compared this Fn immobilization method to commonly used protocols, such as soaking a clean glass in 10 μg/mL Fn solution for 1 h.[151,152] The impact to NIH-3T3 cells, in terms of focal adhesion formation and cellular morphology, appeared very similar.[143,153] Therefore, Fn layers formed via adsorbed onto OTS surfaces serve as the control in this investigation. The Fn appears as protrusions (bright contrast) in a AFM topograph as shown in Figure 8A. As illustrated in the cursor profile in Figure 8B, these Fn protrusions measure 11.6 ± 3.4 nm laterally, with an apparent height of 1.8 ± 0.5 nm. The lower apparent height than the Fn size from the crystal structure[143,154,155] is likely due to the fact the AFM probes may not be able to reach the SAM surface due to the close proximity among neighbor Fn molecules.

Fn Nanogratings Exhibit Strong Guidance to the Orientation and Polarity of NIH 3T3 Cells. The responses of NIH 3T3 cells to the nanograting and control surfaces were investigated by incubating the two supports with cells for 24 h in a Dulbecco's modified Eagle's supplemented with 10% heat-inactivated fetal bovine serum, penicillin (100 U/mL), and streptomycin (100 μg/mL) at 37 °C and 5% CO_2 in a humidified incubator, which is the established condition for forming mature focal adhesion.[156] The cells attached to the two surfaces exhibit significantly different behaviors. First, the orientation of NIH 3T3 cells on Fn nanogratings are parallel to each other, as shown in optical images in Figure 9B. The zoom-in view by AFM (central image in Figure 9B) more clearly reveals the overall topography and orientation. The AFM image in the inset of Figure 9B reveals the direction of Fn nanogratings, which is the same as the cellular orientation. In

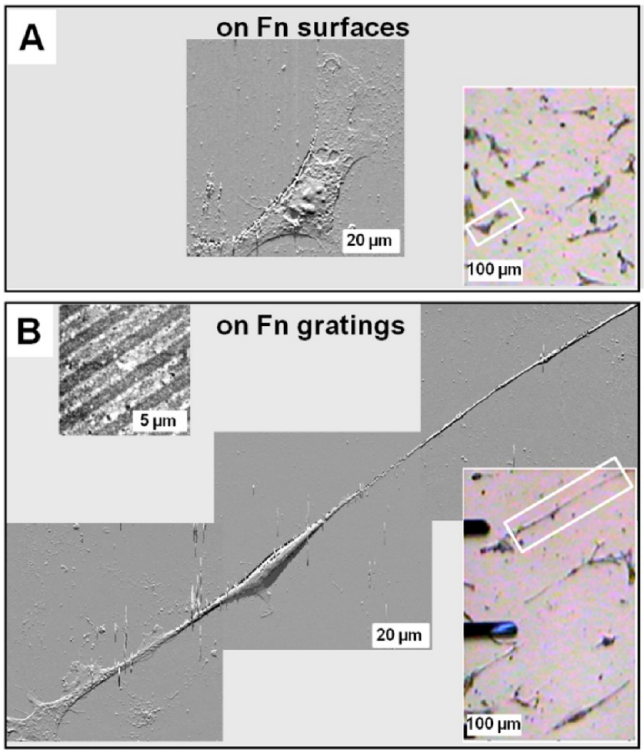

Figure 9. Fn nanogratings guide the orientation and polarization of NIH 3T3 cells. AFM deflection images ($80 \times 80\ \mu m^2$ scan) of a typical NIH 3T3 cell cultured on (A) control and (B) Fn gratings for 24 h. The insets on the right show optical view of NIH 3T3 cells adhered to the indicated surface. The cells selected for AFM imaging were indicated by white rectangle. Inset on the left of (B) is the AFM topograph of the nanograting under the cells. All cells are fixed, dehydrated, and dried before AFM images. AFM images are acquired under contact mode using CSC 38 cantilever with a spring constant of 0.03 N/m.

contrast, cells on the control surface have various orientations, as shown in the optical image in Figure 9A. The comparison demonstrates the strong guidance of Fn nanogratings on the cellular orientation.[148] Among the three sets of experiments and 55 cells imaged, 75% of them were completely parallel to the direction of Fn gratings.

Second, Fn nanogratings lead to strong polarization in cellular morphology. The optical image shown in Figure 9A reveals that the NIH 3T3 cells spread on the control surface, displaying various shapes: from triangular, polygon, to star-like geometries, which is consistent with previous observations.[157] AFM images of individual cells (as shown in the central image in Figure 9A) allow accurate measurement of the polarization ratio. The cell in Figure 9A has a long and a short (perpendicular to long and across the nuclear) axis of 90.3 and 23.5 μm, respectively, a polarization ratio of 3.8 (long/short). Among 61 cells imaged from all control surfaces, the polarization ratio ranges from 2.3 to 5.2. When cultured on Fn gratings, the cells are much more elongated than the control. As shown in Figure 9B, the NIH3T3 measures 330.6 μm long and 9.1 μm wide, a polarization ratio of 36.3. Among nine NIH 3T3 cells imaged with AFM, the polarization ratio ranged from 8.0 to 36.3, which is significantly larger than that of the control.[148] Note that it typically took several frames to capture a complete cell due to this elongation, as shown in Figure 9. A similar effect was also reported using nanogrooves with a depth of 100 nm and the pitch of 500 nm fabricated via laser interference lithography, that is, by spin coating a positive photoresist, S1805, on glass slides and then exposing it to laser.[158] In this case, the rat dermal fibroblasts were elongated with the polarization ratio up to 13.[158] It was concluded that the contact guidance does not exist below the threshold depth of 35 nm because the depth of groove provided a physical constraint to bias the cellular alignment and elongation along the lines.[159] By comparison, our Fn grating was only 3.2 ± 0.5 nm above surrounding. Such a small topographic difference, without using Fn, would not be sufficient to provide physical constraint and guide cellular orientation and morphology.[159] However, with the presence of Fn, the nanolines appear most effective in polarizing cellular morphology, leading to the highest polarization ratio (36.3), and longest filopodium (156 μm) among fibroblasts. Therefore, the guidance is mainly attributed to the Fn functionality and nanolines, in conjunction with the Fn–integrin interactions, not the physical or topographic constraints.

We emphasize that the local structure of Fn is also an important factor in cellular regulation. Polarization of human dermal fibroblasts (HDF) cultured on Fn microline arrays was also reported, by immobilizing Fn on the hexadecanethiol SAM micropattern on gold-coated wafer produced by microcontact printing. The rest of the surface was passivated by 1-mercaptoundec-11-yl hexa(ethylene glycol) SAM. Fn strips are taller than the surrounding PEG regions by 1.8 nm. The cells alignment and elongation were observed when the interline spacing was greater than 17 μm, where the cell only covered one line and became a needlelike shape with a polarization ratio of 10–25.[144] In contrast, there was no preferred polarization if interline spacing was below 10 μm.[144] This result, at first glance, seems to contradict our observations, where interline separation is 0.65 μm. The key is the apparent height of Fn, where in the previous case, the height measured 1.8 nm above surrounding region, in contrast to our value of 3.2 ± 0.5 nm. The Fn in this "short" grating is not as sufficient as the Fn presented in our grating. In other words, the comparison is analogous to strong binding nanolines versus weak binding microlines. The significance of this comparison is the conclusion that functional nanostructures, such as ***potent Fn nanolines***, provide an effective and alternative means to regulate the cellular adhesion, local motion, and morphology, complementary to the methods of topographic controls such as micrograting,[144] deep microgroves,[158–160] gradients substratum with micrometer sized ridges, and trenches.[161]

Fn Gratings Exhibit Preferential Sensing by Filopodia. Filopodia are important in influencing cellular topography and local motion. Filopodia are fingerlike in shape, appearing as actin-rich plasma-membrane protrusions that cells use to explore the environment.[10,162] Using a pre-engineered local environment, that is, nanogratings, we tested to find if the inhomogeneous distribution of Fn as defined by the gratings manifests into a difference in filopodia behavior.[148] One example is shown in Figure 10A, where AFM images could clearly reveal the topography of filopodia and the surface underneath. Where filopodia can be found at the periphery of the cells, larger populations are found at the two ends of the cell, which indicates that the local movement of the cell concentrates at the two ends, thus the elongation. By systematically zooming into the filopodia region at the side of the cell (defined in the frame of Figure 10A), AFM topography reveals the location of tips of these filopodia with respect to the

dx.doi.org/10.1021/bi200880p | *Biochemistry* 2012, 51, 5876–5893

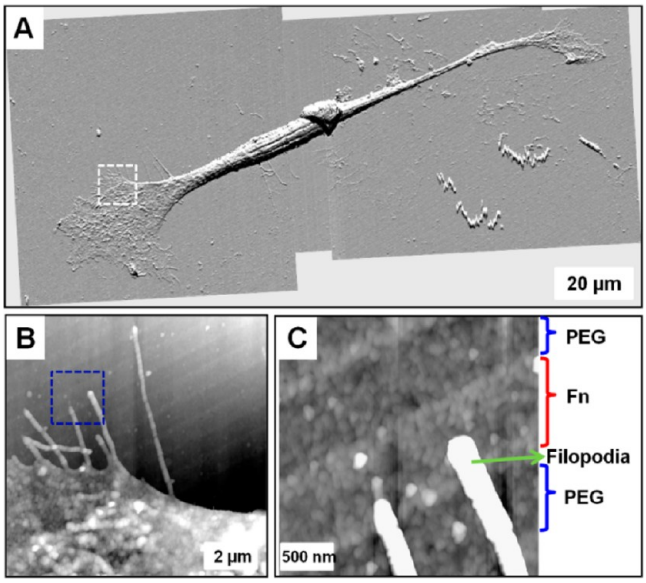

Figure 10. Filopodia exhibit preferred contact with the Fn region over surrounding PEG regions. (A) AFM deflection image of a very narrow NIH 3T3 cell on the Fn nanografting as prepared in Figure 9B. The AFM image is attained by combining three frames in order to cover the entire cell. (B) and (C) are the successive zoom-in views of the filopodia, whose tip always lands onto the Fn regions. AFM images are acquired under contact mode using CSC 38 cantilevers with a spring constant of 0.03 N/m.

grating underneath. All tips landed in the Fn regions of the grating, as shown in Figure 10B,C. Among three cells studied on Fn gratings, this observation remains valid. Although the height difference between Fn grating and surrounding PEG regions is only 3.2 nm, the chemical difference, Fn versus PEG, is sufficient to guide the filopodia movement. Our results are consistent with the knowledge that integrins are found in the tips of filopodia,[163] which explains the preferred binding onto Fn regions. The favored binding to Fn lines over other regions leads to guided local motion in favor of Fn-rich areas, causing cellular extension and migration along the grating directions. This guiding effect is significant in cellular behavior because a key role of filopodia is to promote cell migration and spreading, ultimately leading to morphology evolution.[162] Since the nature of the adhesion is integrin-Fn binding instead of topographic guidance, the binding site could initiate focal adhesion and result in formation of actin stress fibers.[164] Our results provide further evidence that living cells are highly sensitive to local environment at the nanoscale. By using nanotechnology, fabrication of ligands or even biocompatible scaffolds becomes feasible as a new and effective means to direct cell behaviors and functions.

Fn Gratings Guide the Alignment and Spatial Arrangement of Cytoskeleton Actin Stress Fibers. Taking advantage of the high resolution AFM and confocal imaging offer, we have investigated the distribution and alignment of intracellular actin stress fibers, at the central as well periphery regions, in relation to the engineered Fn pattern underneath.[148] As shown in Figure 11A, the control Fn surface, there are six cells within the 210 × 210 μm^2 imaging frame. These cells exhibit different geometries and random orientations, as highlighted by confocal imaging upon fixation and phalloidin stain.[156] Zooming into the selected cells, the confocal image shown in Figure 11B clearly reveals the location, number, and

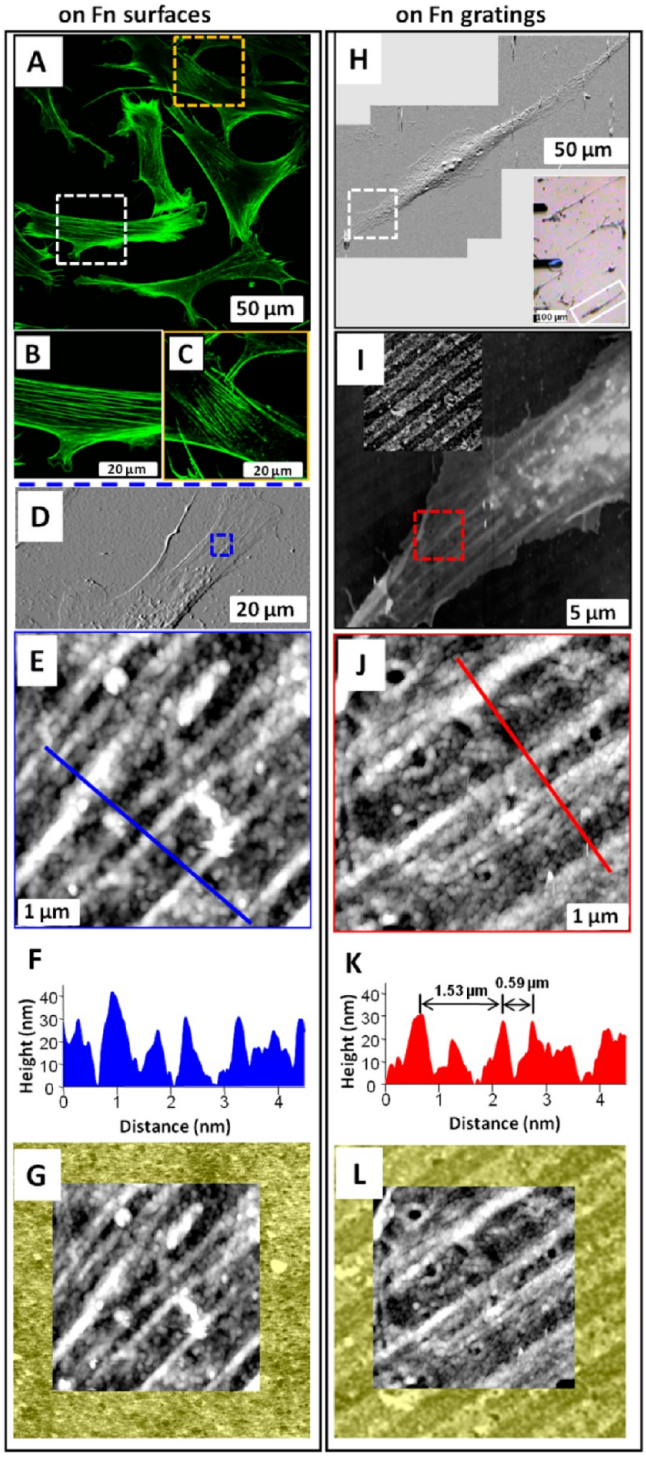

Figure 11. Fn gratings guide the orientation and spatial arrangement of intracellular actin stress fiber. (A–G) NIH 3T3 cells on control surfaces for 24 h. (A) Confocal images of F-actin localization in fixed NIH 3T3 cells on control. The cells were fixed and stained with Alexa fluor 488 labeled phalloidin, and then imaged under a FluoView 1000 system (Olympus America). All confocal images were acquired using a Plan Apo N (60×, N.A. = 1.42) oil immersion bright-field objective. The confocal images were with emission between 500 and 600 nm under an excitation of 488 nm. (B, C) are zoom-in confocal images of actin stress fiber to demonstrate the orientation of actin stress fiber follow the long axis of cell but vary from cell to cell. (D) A 40 × 80 μm^2 AFM deflection of NIH 3T3 cells on control surfaces. (E) Zoom-in AFM topography image of actin stress fiber in a 5 × 5 μm^2 area. (F) is the cursor profile as indicated in E. (G) Overlay of AFM topography

dx.doi.org/10.1021/bi200880p | *Biochemistry* 2012, 51, 5876–5893

Figure 11. continued

images of actin stress fiber with the underneath surface (H–L) NIH 3T3 cells on Fn gratings. (H) The representative AFM deflection image of a NIH 3T3 cell on Fn gratings. The AFM image is attained by combining three frames in order to cover the entire cell. The insets on the right show an optical view of NIH 3T3 cells adhered to Fn gratings. (I) Zoom-in AFM topography image shown actin stress fibers follow cell orientation and parallel to Fn gratings, and the inset is the underlying nanoline arrays of Fn. (J) Higher magnification of AFM topography images of actin stress fibers in a $5 \times 5\ \mu m^2$ area. (K) is the cursor profile as indicated in J. (L) the overlay of AFM topography images of actin stress fiber with underneath Fn gratings, which indicated that the Fn on the edge of the gratings guidance the spatial arrangement of actin stress fibers. AFM images are acquired under contact mode in air using CSC 38 cantilever with a spring constant of 0.03 N/m.

arrangement of actin stress fibers. In this case, actin stress fibers are present as bundles in various locations of cells. The central bundles are aligned ±5° along the cellular orientation. There is a higher population of actin stress fibers at the periphery of the cells, whose long axes may differ from the overall cellular orientation, but follow the direction of local motion. Zooming in to different cells such as in Figure 11C, shorter actin stress fibers than those in Figure 11B are visible, and they are aligned with the orientation of the cell within ±10°. Since many cells do not have a predominant polarization, several bundles of actin fibers could follow the local orientation within the cells (see the triangular cell in the middle right of Figure 11A). In addition, cells do not share a common orientation on the control surface, and actin stress fibers follow the cellular direction and thus vary from cell to cell (note Figure 11B's fibers differ from those in 11C). These observations are consistent with previous reports and were attributed to the results of downstream focal adhesion signaling processes.[156,157,165]

On Fn gratings, cells are polarized along the grating, as discussed previously. Figure 11H displays the AFM deflection image of overall cellular morphology of an individual NIH 3T3 cell on an Fn grating, from which the cellular orientation and boundaries are clearly seen. Upon successive zooming into various regions of the cell, AFM topography images Figure 11I,J reveal that all actin stress fibers are parallel to the long axis of the cell and follow the direction of the Fn grating. This observation suggests that the cytoskeleton reorganization, due to mature focal adhesion, can be guided by the Fn nanolines underneath. Similar alignment was reported using topographic cues,[144,158,166] in comparison to our biochemical nanostructures.

More importantly, high-resolution of AFM topography also allows a 3D view of these parallel actin stress fibers (Figure 11J). For example, height, width, and separation can be extracted from the cursor profiles shown in Figure 11K. Figure 11L displays the overlay of the AFM topography images of actin stress fibers with underlying Fn gratings (acquired before cellular adhesion). ***The actin stress fibers at the peripheral regions are almost superimposed with the Fn nanolines underneath.*** Such a strong guiding effect has not been reported previously, to the best of our knowledge. As a comparison, we displayed the fibroblast on control surfaces in Figure 11G, which reveals no correlation between actin stress fibers and surface structures.

The significance of our work is that Fn gratings, with the height of 3.2 ± 0.5 nm, not only orient actin stress fibers along the grating direction, but also determine the spatial arrangement of actin stress fibers to MATCH the edges or nanolines of

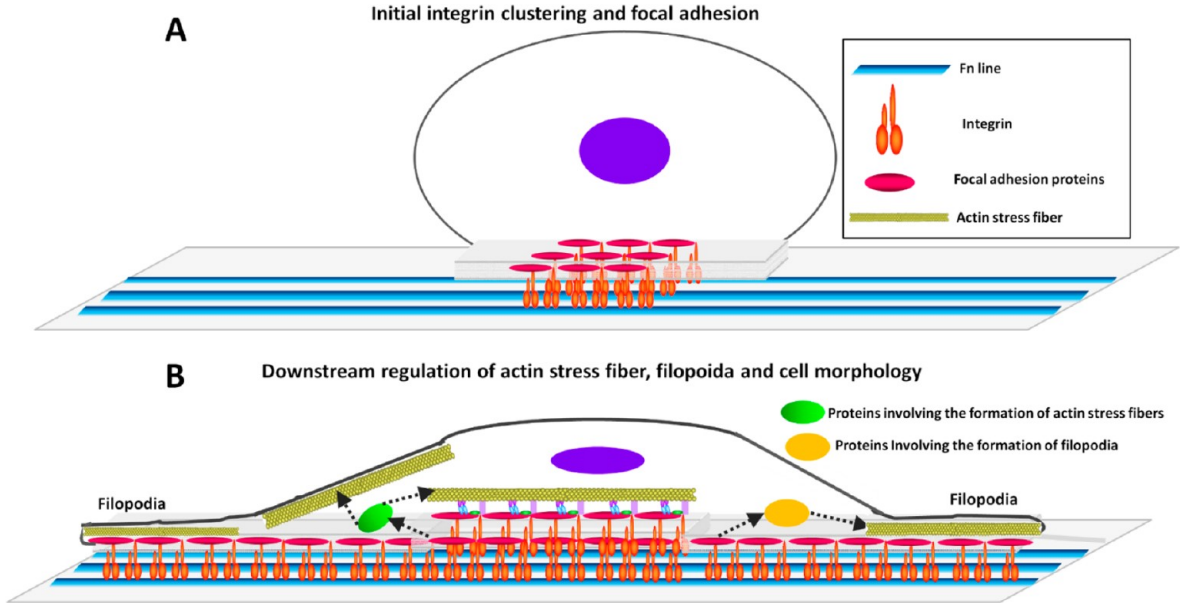

Figure 12. The mechanism of Fn nanograting guided cellular morphology and cytoskeleton rearrangement. (A) Fn nanolines guide the initial integrin clustering and result in the focal adhesion alignment. (B) The initial alignment propagates to the recruitment of integrin-mediated activation of Rho family GTPases (Rho, Rac, and Cdc 42) and leading to actin organization into filopodia and stress fibers. Cdc 42 and Rac dependent activation of PAK kinase blocks MLC kinase and contribute to the filopodia formation, while Rho mediated contractility through ROCK assembles stress fibers. The alignment of focal adhesion leads to actin stress fiber alignment and filopodia parallel to Fn line, which leads to the polarization of cell body, alignment, and elongation.

dx.doi.org/10.1021/bi200880p | *Biochemistry* 2012, 51, 5876–5893

Fn gratings. The strong guidance here is not topographic in nature, as the mere 3.2 nm corrugation of Fn lines is not sufficient to bias the cellular behavior. The key is the potent Fn nanostructure which can bias the Fn-integrin binding, and then the alignment of the integrin clusters.[148] From previous investigations, it is accepted that at the molecular level, integrin mediated focal adhesions are large, dynamic protein complexes that serve as a link between cytoskeleton of a cell and the ECM.[163,164,167−169] Our observation that nanolines could guide intracellular actin stress fibers direction and orientation of cells, as well as bias filopodia sensing, is consistent with the concept that substrate biochemistry can regulate focal adhesion and hence cytoskeleton orientation, and cellular topography and behavior. This approach complements and enhances previously reported guidance using topographic cues.[160,170,171]

Rationalizing the Observed Guidance by Nanostructures. Combining our observations with the knowledge of the integrin mediated cellular signaling mechanism, we attempt to rationalize the observed guiding effect of Fn nanogratings, as shown in Figure 12. Upon contact with the Fn lines, the integrin receptors located within the membrane of NIH 3T3 cells can migrate and bind with Fn underneath. The high local concentration of Fn along the grating lines does bias the integrin binding, guiding the initial integrin clustering and resulting in the focal adhesion alignment, as illustrated in Figure 12A. This initial event could manifest into downstream processes, such as in Figure 12B. Clustering of integrin initiated by ligand binding results in recruitment of focal adhesion proteins such as tensin and tyrosine kinases to the integrin clusters, and then mediates further downstream cell signaling leading to cell adhesion, migration, and gene expression.[10,167,168] For example, the integrin-Fn clustering along the grating initiates the biased focal adhesion assembly and activation of Rho family GTPases such as Rho, Rac, and Cdc42.[172] These three molecules are very important for the adhesion dependent actin polymerization. Rho mediated contractility though ROCK leads to formation of actin stress fibers.[167,172−174] Rac and Cdc42, though regulation of actin dynamics, contribute to formation of the forward protrusion, such as filopodia,[172,174] whose evolution during cellular spreading is critical in regulating morphology, that is, the alignment and elongation of the cells on gratings.

Comparison of the guiding effect of our Fn nanogratings to previously reported microstructure indicates that engineered nanostructure of Fn provides an alternative and more potent guidance for fibroblast than previous means via physical constraints such as microgrooves. The key is to ensure the presentation of Fn could preserve the potency of the protein. In our nanolines with a height of 3.2 ± 0.5 nm, the Fn gratings exhibit the strongest effects of cellular polarization, biased filopodia sensing, and alignment of intracellular actin stress fibers. More importantly, the actin stress fibers at the peripheral of cells are superpositioned with the Fn nanolines underneath. The strong guidance is also an indication that the integrin mediated process is the most important and relatively fast event in the cellular adhesion, local motion, and morphology, among fibroblasts. We infer that similar guiding effects may prove potent and effective for other cell types, such as endothelial cells[102,141,142,175,176] and human mesenchymal stem cells,[139,177,178] where ECM-integrin mediated processes dominate. Therefore, we encourage researchers to consider applying the nanoengineered structure of ECM protein to regulate cellular function via biochemical cues instead of topography and physical cues.

■ CONCLUDING REMARKS AND FUTURE PROSPECTIVES

The ability to investigate and control cellular signaling processes is of great importance in science and technology. Molecular level investigation of cellular signaling cascades provides fundamental information about cellular behavior at the single cell level, and as such facilitates our understanding of their collective behavior at high levels, including disease formation and functions of tissues and organs. This current topic introduces a new alternative: engineered nanostructures with designed geometry and chemical functionality. The designs are based on the requirements of specific cellular signaling processes, such as antibody-mediated mast cell activation, or focal adhesion among fibroblasts. The key is to match both the geometry and biochemical reactions dictated by the ligand-membrane receptor interactions. For the two processes discussed, nanogrids of DNP with 20 nm separation and nanolines of Fn were designed and produced, respectively. The regulation efficacy appears to be very high, prominent in comparison to previously used cues. We envision that this report would trigger further effort for regulation of other cell types and corresponding signaling processes and cellular functions. The outcomes from use of nanobiotechnology push the boundaries of technological capabilities and provide substantial new insights into regulation of cellular signaling processes and further cell behaviors. Nanoengineered surfaces also can be used for scaffold design, offering the potential to induce desired phenotype and genotype for tissue-engineering applications.

■ AUTHOR INFORMATION

Corresponding Author

*Phone: (530) 754-9678. Fax: (530) 754-8557. E-mail: liu@chem.ucdavis.edu.

Funding

This work was supported by National Science Foundation (CHE-0809977), National Institutes of Health (CA102537, CA151366), and CRCC (Cancer Research Coordination Committee) Research Grant.

Notes

The authors declare no competing financial interest.

■ ACKNOWLEDGMENTS

This work was supported by the University of California, Davis, National Science Foundation (CHE-0809977), W. M. Keck Foundation, and CRCC (Cancer Research Coordination Committee) Research Grant. We thank Drs. Fu-Tong Liu and Huan-Yuan Chen for their helpful discussions regarding mast cell activation, and Dr. Yi-Ping Shih, Ms. Nai-Ning Yin, and Ms. Susan Stagner for their assistance in preparation of this manuscript.

■ ABBREVIATIONS USED

AFM, atomic force microscopy; DMF, *N*,*N*-dimethylformamide; DNP, dinitrophenyl; DNP-thiol, 2,4-dinitrophenylated alkanethiol; DNP-BSA, 2,4-dinitrophenylated bovine serum albumin; ECM, extracellular matrices; Fn, fibronectin; IgE, immunoglobulin E; ITAM, immunoreceptor tyrosine-based activation motif; LYZ, lysozyme; μCP, microcontact printing;

C18, octadecanethiol; OTS, octadecyltrichlorosilane; PBS, phosphate buffered saline; PDMS, poly(dimethylsiloxane); PEG-silane, 2-[methoxy-(polyethyleneoxy)propyl]-trichlorosilane; RBL, rat basophilic leukemia; SEM, scanning electron microscope; SAMs, self-assembled monolayers

REFERENCES

(1) Pawson, T., and Scott, J. D. (1997) Signaling through scaffold, anchoring, and adaptor proteins. *Science 278*, 2075−2080.

(2) Brown, D. A., and London, E. (1998) Functions of lipid rafts in biological membranes. *Annu. Rev. Cell Dev. Biol. 14*, 111−136.

(3) Simons, K., and Toomre, D. (2000) Lipid rafts and signal transduction. *Nat. Rev. Mol. Cell Biol. 1*, 31−39.

(4) Pierce, K. L., Premont, R. T., and Lefkowitz, R. J. (2002) Seven-transmembrane receptors. *Nat. Rev. Mol. Cell Biol. 3*, 639−650.

(5) Samelson, L. E. (2002) Signal transduction mediated by the T cell antigen receptor: The role of adapter proteins. *Annu. Rev. Immunol. 20*, 371−394.

(6) Edelman, G. M., and Crossin, K. L. (1991) Cell-adhesion molecules - Implications for a molecular histology. *Annu. Rev. Biochem. 60*, 155−190.

(7) Clark, E. A., and Brugge, J. S. (1995) Integrins and signal-transduction pathways - the road taken. *Science 268*, 233−239.

(8) Gumbiner, B. M. (1996) Cell adhesion: The molecular basis of tissue architecture and morphogenesis. *Cell 84*, 345−357.

(9) Cukierman, E., Pankov, R., Stevens, D. R., and Yamada, K. M. (2001) Taking cell-matrix adhesions to the third dimension. *Science 294*, 1708−1712.

(10) Geiger, B., Bershadsky, A., Pankov, R., and Yamada, K. M. (2001) Transmembrane extracellular matrix-cytoskeleton crosstalk. *Nat. Rev. Mol. Cell Biol. 2*, 793−805.

(11) Lauffenburger, D. A., and Horwitz, A. F. (1996) Cell migration: A physically integrated molecular process. *Cell 84*, 359−369.

(12) Palecek, S. P., Loftus, J. C., Ginsberg, M. H., Lauffenburger, D. A., and Horwitz, A. F. (1997) Integrin-ligand binding properties govern cell migration speed through cell-substratum adhesiveness. *Nature 385*, 537−540.

(13) Hood, J. D., and Cheresh, D. A. (2002) Role of integrins in cell invasion and migration. *Nat. Rev. Cancer 2*, 91−100.

(14) Taipale, J., and KeskiOja, J. (1997) Growth factors in the extracellular matrix. *FASEB J. 11*, 51−59.

(15) Garcia, A. J., Vega, M. D., and Boettiger, D. (1999) Modulation of cell proliferation and differentiation through substrate-dependent changes in fibronectin conformation. *Mol. Biol. Cell 10*, 785−798.

(16) Mammen, M., Choi, S. K., and Whitesides, G. M. (1998) Polyvalent interactions in biological systems: Implications for design and use of multivalent ligands and inhibitors. *Angew. Chem., Int. Ed. 37*, 2755−2794.

(17) Cairo, C. W., Gestwicki, J. E., Kanai, M., and Kiessling, L. L. (2002) Control of multivalent interactions by binding epitope density. *J. Am. Chem. Soc. 124*, 1615−1619.

(18) Kitov, P. I., and Bundle, D. R. (2003) On the nature of the multivalency effect: A thermodynamic model. *J. Am. Chem. Soc. 125*, 16271−16284.

(19) Kisiday, J., Jin, M., Kurz, B., Hung, H., Semino, C., Zhang, S., and Grodzinsky, A. J. (2002) Self-assembling peptide hydrogel fosters chondrocyte extracellular matrix production and cell division: Implications for cartilage tissue repair. *Proc. Natl. Acad. Sci. U. S. A. 99*, 9996−10001.

(20) Li, W. J., Laurencin, C. T., Caterson, E. J., Tuan, R. S., and Ko, F. K. (2002) Electrospun nanofibrous structure: A novel scaffold for tissue engineering. *J. Biomed. Mater. Res. 60*, 613−621.

(21) Shin, H., Jo, S., and Mikos, A. G. (2003) Biomimetic materials for tissue engineering. *Biomaterials 24*, 4353−4364.

(22) Lutolf, M. P., and Hubbell, J. A. (2005) Synthetic biomaterials as instructive extracellular microenvironments for morphogenesis in tissue engineering. *Nat. Biotechnol. 23*, 47−55.

(23) Desai, T. A. (2000) Micro- and nanoscale structures for tissue engineering constructs. *Med. Eng. Phys. 22*, 595−606.

(24) Khademhosseini, A., Langer, R., Borenstein, J., and Vacanti, J. P. (2006) Microscale technologies for tissue engineering and biology. *Proc. Natl. Acad. Sci. U.S.A. 103*, 2480−2487.

(25) Bettinger, C. J., Langer, R., and Borenstein, J. T. (2009) Engineering substrate topography at the micro- and nanoscale to control cell function. *Angew. Chem., Int. Ed. 48*, 5406−5415.

(26) Dvir, T., Timko, B. P., Kohane, D. S., and Langer, R. (2011) Nanotechnological strategies for engineering complex tissues. *Nat. Nanotechnol. 6*, 13−22.

(27) Strong, L. E., and Kiessling, L. L. (1999) A general synthetic route to defined, biologically active multivalent arrays. *J. Am. Chem. Soc. 121*, 6193−6196.

(28) Badjic, J. D., Nelson, A., Cantrill, S. J., Turnbull, W. B., and Stoddart, J. F. (2005) Multivalency and cooperativity in supramolecular chemistry. *Acc. Chem. Res. 38*, 723−732.

(29) Weissleder, R., Kelly, K., Sun, E. Y., Shtatland, T., and Josephson, L. (2005) Cell-specific targeting of nanoparticles by multivalent attachment of small molecules. *Nat. Biotechnol. 23*, 1418−1423.

(30) Arnold, M., Cavalcanti-Adam, E. A., Glass, R., Blummel, J., Eck, W., Kantlehner, M., Kessler, H., and Spatz, J. P. (2004) Activation of integrin function by nanopatterned adhesive interfaces. *ChemPhysChem 5*, 383−388.

(31) Torres, A. J., Wu, M., Holowka, D., and Baird, B. (2008) Nanobiotechnology and cell biology: Micro- and nanofabricated surfaces to investigate receptor-mediated signaling. *Annu. Rev. Biophys. 37*, 265−288.

(32) Deng, Z., Weng, I. C., Li, J. R., Chen, H. Y., Liu, F. T., and Liu, G. Y. (2011) Engineered nanostructures of antigen provide an effective means for regulating mast cell activation. *ACS Nano 5*, 8672−8683.

(33) Geiger, B., Spatz, J. P., and Bershadsky, A. D. (2009) Environmental sensing through focal adhesions. *Nat. Rev. Mol. Cell Biol. 10*, 21−33.

(34) Beaven, M. A., and Metzger, H. (1993) Signal-transduction by Fc-receptors - the Fc-epsilon-RI case. *Immunol. Today 14*, 222−226.

(35) Kinet, J. P. (1999) The high-affinity IgE receptor (Fc epsilon RI): From physiology to pathology. *Annu. Rev. Immunol. 17*, 931−972.

(36) Turner, H., and Kinet, J. P. (1999) Signalling through the high-affinity IgE receptor Fc epsilon RI. *Nature 402*, B24−B30.

(37) Gilfillan, A. M., and Tkaczyk, C. (2006) Integrated signalling pathways for mast-cell activation. *Nat. Rev. Immunol. 6*, 218−230.

(38) Schwartz, M. A., Schaller, M. D., and Ginsberg, M. H. (1995) Integrins: Emerging paradigms of signal transduction. *Annu. Rev. Cell Dev. Biol. 11*, 549−599.

(39) Burridge, K., and ChrzanowskaWodnicka, M. (1996) Focal adhesions, contractility, and signaling. *Annu. Rev. Cell Dev. Biol. 12*, 463−518.

(40) Giancotti, F. G., and Ruoslahti, E. (1999) Transduction - integrin signaling. *Science 285*, 1028−1032.

(41) Sharma, B. B., Apgar, J. R., and Liu, F. T. (2002) Mast cells - Receptors, secretagogues, and signaling. *Clin. Rev. Allergy Immunol. 22*, 119−148.

(42) Wilson, B. S., Pfeiffer, J. R., and Oliver, J. M. (2002) Fc epsilon RI signaling observed from the inside of the mast cell membrane. *Mol. Immunol. 38*, 1259−1268.

(43) Rivera, J., and Gilfillan, A. M. (2006) Molecular regulation of mast cell activation. *J. Allergy Clin. Immunol. 117*, 1214−1225.

(44) Holowka, D., Sil, D., Torigoe, C., and Baird, B. (2007) Insights into immunoglobulin E receptor signaling from structurally defined ligands. *Immunol. Rev. 217*, 269−279.

(45) MacGlashan, D. (2008) IgE receptor and signal transduction in mast cells and basophils. *Curr. Opin. Immunol. 20*, 717−723.

(46) Seagrave, J., Pfeiffer, J. R., Wofsy, C., and Oliver, J. M. (1991) Relationship of IgE receptor topography to secretion in RBL-2H3 mast-cells. *J. Cell. Physiol. 148*, 139−151.

(47) Baird, E. J., Holowka, D., Coates, G. W., and Baird, B. (2003) Highly effective poly(ethylene glycol) architectures for specific

inhibition of immune receptor activation. *Biochemistry 42*, 12739−12748.
(48) Hynes, R. O. (2002) Integrins: Bidirectional, allosteric signaling machines. *Cell 110*, 673−687.
(49) Miyamoto, S., Akiyama, S. K., and Yamada, K. M. (1995) Synergistic roles for receptor occupancy and aggregation in integrin transmembrane function. *Science 267*, 883−885.
(50) Miyamoto, S., Teramoto, H., Coso, O. A., Gutkind, J. S., Burbelo, P. D., Akiyama, S. K., and Yamada, K. M. (1995) Integrin function - Molecular hierarchies of cytoskeletal and signaling molecules. *J. Cell Biol. 131*, 791−805.
(51) Miyamoto, S., Teramoto, H., Gutkind, J. S., and Yamada, K. M. (1996) Integrins can collaborate with growth factors for phosphorylation of receptor tyrosine kinases and MAP kinase activation: Roles of integrin aggregation and occupancy of receptors. *J. Cell Biol. 135*, 1633−1642.
(52) Leahy, D. J., Aukhil, I., and Erickson, H. P. (1996) 2.0 angstrom crystal structure of a four-domain segment of human fibronectin encompassing the RGD loop and synergy region. *Cell 84*, 155−164.
(53) Maheshwari, G., Brown, G., Lauffenburger, D. A., Wells, A., and Griffith, L. G. (2000) Cell adhesion and motility depend on nanoscale RGD clustering. *J. Cell Sci. 113*, 1677−1686.
(54) Davis, D. M., Chiu, I., Fassett, M., Cohen, G. B., Mandelboim, O., and Strominger, J. L. (1999) The human natural killer cell immune synapse. *Proc. Natl. Acad. Sci. U. S. A. 96*, 15062−15067.
(55) Bromley, S. K., Burack, W. R., Johnson, K. G., Somersalo, K., Sims, T. N., Sumen, C., Davis, M. M., Shaw, A. S., Allen, P. M., and Dustin, M. L. (2001) The immunological synapse. *Annu. Rev. Immunol. 19*, 375−396.
(56) Lee, K. H., Holdorf, A. D., Dustin, M. L., Chan, A. C., Allen, P. M., and Shaw, A. S. (2002) T cell receptor signaling precedes immunological synapse formation. *Science 295*, 1539−1542.
(57) Davis, D. M., and Dustin, M. L. (2004) What is the importance of the immunological synapse? *Trends Immunol. 25*, 323−327.
(58) Mossman, K. D., Campi, G., Groves, J. T., and Dustin, M. L. (2005) Altered TCR signaling from geometrically repatterned immunological synapses. *Science 310*, 1191−1193.
(59) Dustin, M. L., Olszowy, M. W., Holdorf, A. D., Li, J., Bromley, S., Desai, N., Widder, P., Rosenberger, F., van der Merwe, P. A., Allen, P. M., and Shaw, A. S. (1998) A novel adaptor protein orchestrates receptor patterning and cytoskeletal polarity in T-cell contacts. *Cell 94*, 667−677.
(60) Wild, M. K., Cambiaggi, A., Brown, M. H., Davies, E. A., Ohno, H., Saito, T., and van der Merwe, P. A. (1999) Dependence of T cell antigen recognition on the dimensions of an accessory receptor-ligand complex. *J. Exp. Med. 190*, 31−41.
(61) Dustin, M. L., and Colman, D. R. (2002) Neural and immunological synaptic relations. *Science 298*, 785−789.
(62) Wilbur, J. L., Kumar, A., Kim, E., and Whitesides, G. M. (1994) Microfabrication by microcontact printing of self-assembled monolayers. *Adv. Mater. 6*, 600−604.
(63) Jackman, R. J., Wilbur, J. L., and Whitesides, G. M. (1995) Fabrication of submicrometer features on curved substrates by microcontact printing. *Science 269*, 664−666.
(64) Xia, Y. N., Mrksich, M., Kim, E., and Whitesides, G. M. (1995) Microcontact printing of octadecylsiloxane on the surface of silicon dioxide and its application in microfabrication. *J. Am. Chem. Soc. 117*, 9576−9577.
(65) Xia, Y. N., and Whitesides, G. M. (1998) Soft lithography. *Annu. Rev. Mater. Sci. 28*, 153−184.
(66) Smith, R. K., Lewis, P. A., and Weiss, P. S. (2004) Patterning self-assembled monolayers. *Prog. Surf. Sci. 75*, 1−68.
(67) Haynes, C. L., and Van Duyne, R. P. (2001) Nanosphere lithography: A versatile nanofabrication tool for studies of size-dependent nanoparticle optics. *J. Phys. Chem. B 105*, 5599−5611.
(68) Yang, S. M., Jang, S. G., Choi, D. G., Kim, S., and Yu, H. K. (2006) Nanomachining by colloidal lithography. *Small 2*, 458−475.
(69) Wood, M. A. (2007) Colloidal lithography and current fabrication techniques producing in-plane nanotopography for biological applications. *J. R. Soc. Interface 4*, 1−17.
(70) Li, J. R., and Garno, J. C. (2008) Elucidating the role of surface hydrolysis in preparing organosilane nanostructures via particle lithography. *Nano Lett. 8*, 1916−1922.
(71) Zhang, J. H., Li, Y. F., Zhang, X. M., and Yang, B. (2010) Colloidal self-assembly meets nanofabrication: From two-dimensional colloidal crystals to nanostructure arrays. *Adv. Mater. 22*, 4249−4269.
(72) Liu, G. Y., Xu, S., and Qian, Y. L. (2000) Nanofabrication of self-assembled monolayers using scanning probe lithography. *Acc. Chem. Res. 33*, 457−466.
(73) Kramer, S., Fuierer, R. R., and Gorman, C. B. (2003) Scanning probe lithography using self-assembled monolayers. *Chem. Rev. 103*, 4367−4418.
(74) Ginger, D. S., Zhang, H., and Mirkin, C. A. (2004) The evolution of dip-pen nanolithography. *Angew. Chem., Int. Ed. 43*, 30−45.
(75) Wouters, D., and Schubert, U. S. (2004) Nanolithography and nanochemistry: Probe-related patterning techniques and chemical modification for nanometer-sized devices. *Angew. Chem., Int. Ed. 43*, 2480−2495.
(76) Tseng, A. A., Notargiacomo, A., and Chen, T. P. (2005) Nanofabrication by scanning probe microscope lithography: A review. *J. Vac. Sci. Technol. B 23*, 877−894.
(77) Garcia, R., Martinez, R. V., and Martinez, J. (2006) Nano-chemistry and scanning probe nanolithographies. *Chem. Soc. Rev. 35*, 29−38.
(78) Kaholek, M., Lee, W. K., LaMattina, B., Caster, K. C., and Zauscher, S. (2004) Fabrication of stimulus-responsive nanopatterned polymer brushes by scanning-probe lithography. *Nano Lett. 4*, 373−376.
(79) Headrick, J. E., Armstrong, M., Cratty, J., Hammond, S., Sheriff, B. A., and Berrie, C. L. (2005) Nanoscale patterning of alkyl monolayers on silicon using the atomic force microscope. *Langmuir 21*, 4117−4122.
(80) Shi, J. J., Chen, J. X., and Cremer, P. S. (2008) Sub-100 nm patterning of supported bilayers by nanoshaving lithography. *J. Am. Chem. Soc. 130*, 2718−2719.
(81) Rosa, L. G., Jiang, J. Y., Lima, O. V., Xiao, J., Utreras, E., Dowben, P. A., and Tan, L. (2009) Selective nanoshaving of self-assembled monolayers of 2-(4-pyridylethyl)triethoxysilane. *Mater. Lett. 63*, 961−964.
(82) Xu, S., and Liu, G. Y. (1997) Nanometer-scale fabrication by simultaneous nanoshaving and molecular self-assembly. *Langmuir 13*, 127−129.
(83) Xu, S., Laibinis, P. E., and Liu, G. Y. (1998) Accelerating the kinetics of thiol self-assembly on gold - A spatial confinement effect. *J. Am. Chem. Soc. 120*, 9356−9361.
(84) Wadu-Mesthrige, K., Xu, S., Amro, N. A., and Liu, G. Y. (1999) Fabrication and imaging of nanometer-sized protein patterns. *Langmuir 15*, 8580−8583.
(85) Xu, S., Miller, S., Laibinis, P. E., and Liu, G. Y. (1999) Fabrication of nanometer scale patterns within self-assembled monolayers by nanografting. *Langmuir 15*, 7244−7251.
(86) Amro, N. A., Xu, S., and Liu, G. Y. (2000) Patterning surfaces using tip-directed displacement and self-assembly. *Langmuir 16*, 3006−3009.
(87) Liu, J. F., Cruchon-Dupeyrat, S., Garno, J. C., Frommer, J., and Liu, G. Y. (2002) Three-dimensional nanostructure construction via nanografting: Positive and negative pattern transfer. *Nano Lett. 2*, 937−940.
(88) Liu, M. Z., Amro, N. A., Chow, C. S., and Liu, G. Y. (2002) Production of nanostructures of DNA on surfaces. *Nano Lett. 2*, 863−867.
(89) Garno, J. C., Yang, Y. Y., Amro, N. A., Cruchon-Dupeyrat, S., Chen, S. W., and Liu, G. Y. (2003) Precise positioning of nanoparticles on surfaces using scanning probe lithography. *Nano Lett. 3*, 389−395.

(90) Liu, M., Amro, N. A., and Liu, G. Y. (2008) Nanografting for surface physical chemistry. *Annu. Rev. Phys. Chem. 59*, 367−386.
(91) Piner, R. D., Zhu, J., Xu, F., Hong, S. H., and Mirkin, C. A. (1999) "Dip-pen" nanolithography. *Science 283*, 661−663.
(92) Hong, S. H., Zhu, J., and Mirkin, C. A. (1999) Multiple ink nanolithography: Toward a multiple-pen nano-plotter. *Science 286*, 523−525.
(93) Demers, L. M., Ginger, D. S., Park, S. J., Li, Z., Chung, S. W., and Mirkin, C. A. (2002) Direct patterning of modified oligonucleotides on metals and insulators by dip-pen nanolithography. *Science 296*, 1836−1838.
(94) Lee, K. B., Park, S. J., Mirkin, C. A., Smith, J. C., and Mrksich, M. (2002) Protein nanoarrays generated by dip-pen nanolithography. *Science 295*, 1702−1705.
(95) Garcia, R., Calleja, M., and Perez-Murano, F. (1998) Local oxidation of silicon surfaces by dynamic force microscopy: Nanofabrication and water bridge formation. *Appl. Phys. Lett. 72*, 2295−2297.
(96) Held, R., Vancura, T., Heinzel, T., Ensslin, K., Holland, M., and Wegscheider, W. (1998) In-plane gates and nanostructures fabricated by direct oxidation of semiconductor heterostructures with an atomic force microscope. *Appl. Phys. Lett. 73*, 262−264.
(97) Maoz, R., Frydman, E., Cohen, S. R., and Sagiv, J. (2000) Constructive nanolithography: Site-defined silver self-assembly on nanoelectrochemically patterned monolayer templates. *Adv. Mater. 12*, 424−429.
(98) Maoz, R., Frydman, E., Cohen, S. R., and Sagiv, J. (2000) "Constructive nanolithography": Inert monolayers as patternable templates for in-situ nanofabrication of metal-semiconductor-organic surface structures - A generic approach. *Adv. Mater. 12*, 725−731.
(99) Liu, S. T., Maoz, R., Schmid, G., and Sagiv, J. (2002) Template guided self-assembly of [Au5(5)] clusters on nanolithographically defined monolayer patterns. *Nano Lett. 2*, 1055−1060.
(100) Liu, S. T., Maoz, R., and Sagiv, J. (2004) Planned nanostructures of colloidal gold via self-assembly on hierarchically assembled organic bilayer template patterns with in-situ generated terminal amino functionality. *Nano Lett. 4*, 845−851.
(101) Liu, G. Y., and Amro, N. A. (2002) Positioning protein molecules on surfaces: A nanoengineering approach to supramolecular chemistry. *Proc. Natl. Acad. Sci. U.S.A. 99*, 5165−5170.
(102) Mrksich, M., Chen, C. S., Xia, Y. N., Dike, L. E., Ingber, D. E., and Whitesides, G. M. (1996) Controlling cell attachment on contoured surfaces with self-assembled monolayers of alkanethiolates on gold. *Proc. Natl. Acad. Sci. U.S.A. 93*, 10775−10778.
(103) Mrksich, M., and Whitesides, G. M. (1996) Using self-assembled monolayers to understand the interactions of man-made surfaces with proteins and cells. *Annu. Rev. Biophys. Biomol. Struct. 25*, 55−78.
(104) Bernard, A., Delamarche, E., Schmid, H., Michel, B., Bosshard, H. R., and Biebuyck, H. (1998) Printing patterns of proteins. *Langmuir 14*, 2225−2229.
(105) Chen, C. S., Mrksich, M., Huang, S., Whitesides, G. M., and Ingber, D. E. (1998) Micropatterned surfaces for control of cell shape, position, and function. *Biotechnol. Prog. 14*, 356−363.
(106) Kane, R. S., Takayama, S., Ostuni, E., Ingber, D. E., and Whitesides, G. M. (1999) Patterning proteins and cells using soft lithography. *Biomaterials 20*, 2363−2376.
(107) Bernard, A., Renault, J. P., Michel, B., Bosshard, H. R., and Delamarche, E. (2000) Microcontact printing of proteins. *Adv. Mater. 12*, 1067−1070.
(108) Zhang, M. Q., Desai, T., and Ferrari, M. (1998) Proteins and cells on PEG immobilized silicon surfaces. *Biomaterials 19*, 953−960.
(109) Kingshott, P., and Griesser, H. J. (1999) Surfaces that resist bioadhesion. *Curr. Opin. Solid State Mater. Sci. 4*, 403−412.
(110) Faucheux, N., Schweiss, R., Lutzow, K., Werner, C., and Groth, T. (2004) Self-assembled monolayers with different terminating groups as model substrates for cell adhesion studies. *Biomaterials 25*, 2721−2730.
(111) Senaratne, W., Takada, K., Das, R., Cohen, J., Baird, B., Abruna, H. D., and Ober, C. K. (2006) Dinitrophenyl ligand substrates and their application to immunosensors. *Biosens. Bioelectron. 22*, 63−70.
(112) Senaratne, W., Sengupta, P., Jakubek, V., Holowka, D., Ober, C. K., and Baird, B. (2006) Functionalized surface arrays for spatial targeting of immune cell signaling. *J. Am. Chem. Soc. 128*, 5594−5595.
(113) Oliver, J. M., Seagrave, J. C., Pfeiffer, J. R., Feibig, M. L., and Deanin, G. G. (1985) Surface functions during mitosis in rat basophilic leukemia-cells. *J. Cell Biol. 101*, 2156−2166.
(114) Pfeiffer, J. R., Seagrave, J. C., Davis, B. H., Deanin, G. G., and Oliver, J. M. (1985) Membrane and cytoskeletal changes associated with IgE-mediated serotonin release from rat basophilic leukemia-cells. *J. Cell Biol. 101*, 2145−2155.
(115) Deanin, G. G., Pfeiffer, J. R., Cutts, J. L., Fore, M. L., and Oliver, J. M. (1991) Isoprenoid pathway activity is required for IgE receptor-mediated, tyrosine kinase-coupled transmembrane signaling in permeabilized RBL-2H3 rat basophilic leukemia-cells. *Cell Regul. 2*, 627−640.
(116) Deng, Z., Zink, T., Chen, H. Y., Walters, D., Liu, F. T., and Liu, G. Y. (2009) Impact of actin rearrangement and degranulation on the membrane structure of primary mast cells: a combined atomic force and laser scanning confocal microscopy investigation. *Biophys. J. 96*, 1629−1639.
(117) Haynes, C. A., and Norde, W. (1995) Structures and stabilities of adsorbed proteins. *J. Colloid Interface Sci. 169*, 313−328.
(118) Fernandez-Lafuente, R., Armisen, P., Sabuquillo, P., Fernandez-Lorente, G., and Guisan, J. M. (1998) Immobilization of lipases by selective adsorption on hydrophobic supports. *Chem. Phys. Lipids 93*, 185−197.
(119) Rusmini, F., Zhong, Z. Y., and Feijen, J. (2007) Protein immobilization strategies for protein biochips. *Biomacromolecules 8*, 1775−1789.
(120) Yu, J. J., Tan, Y. H., Li, X., Kuo, P. K., and Liu, G. Y. (2006) A nanoengineering approach to regulate the lateral heterogeneity of self-assembled monolayers. *J. Am. Chem. Soc. 128*, 11574−11581.
(121) Bu, D. L., Mullen, T. J., and Liu, G. Y. (2010) Regulation of local structure and composition of binary disulfide and thiol self-assembled monolayers using nanografting. *ACS Nano 4*, 6863−6873.
(122) Sahara, N., Siraganian, R. P., and Oliver, C. (1990) Morphological changes induced by the calcium ionophore A23187 in rat basophilic leukemia (2H3) cells. *J. Histochem. Cytochem. 38*, 975−983.
(123) Zink, T., Deng, Z., Chen, H., Yu, L., Liu, F. T., and Liu, G. Y. (2008) High-resolution three-dimensional imaging of the rich membrane structures of bone marrow-derived mast cells. *Ultramicroscopy 109*, 22−31.
(124) Nishida, K., Yamasaki, S., Ito, Y., Kabu, K., Hattori, K., Tezuka, T., Nishizumi, H., Kitamura, D., Goitsuka, R., Geha, R. S., Yamamoto, T., Yagi, T., and Hirano, T. (2005) Fc epsilon RI-mediated mast cell degranulation requires calcium-independent microtubule-dependent translocation of granules to the plasma membrane. *J. Cell Biol. 170*, 115−126.
(125) Bongrand, P. (1999) Ligand-receptor interactions. *Rep. Prog. Phys. 62*, 921−968.
(126) Jeppesen, C., Wong, J. Y., Kuhl, T. L., Israelachvili, J. N., Mullah, N., Zalipsky, S., and Marques, C. M. (2001) Impact of polymer tether length on multiple ligand-receptor bond formation. *Science 293*, 465−468.
(127) Jung, H. S., Yang, T., Lasagna, M. D., Shi, J. J., Reinhart, G. D., and Cremer, P. S. (2008) Impact of hapten presentation on antibody binding at lipid membrane interfaces. *Biophys. J. 94*, 3094−3103.
(128) Jung, H., Robison, A. D., and Cremer, P. S. (2009) Multivalent ligand-receptor binding on supported lipid bilayers. *J. Struct. Biol. 168*, 90−94.
(129) Jayaraman, N. (2009) Multivalent ligand presentation as a central concept to study intricate carbohydrate-protein interactions. *Chem. Soc. Rev. 38*, 3463−3483.

(130) Wong, J. Y., Kuhl, T. L., Israelachvili, J. N., Mullah, N., and Zalipsky, S. (1997) Direct measurement of a tethered ligand-receptor interaction potential. *Science 275*, 820−822.
(131) Kulin, S., Kishore, R., Hubbard, J. B., and Helmerson, K. (2002) Real-time measurement of spontaneous antigen-antibody dissociation. *Biophys. J. 83*, 1965−1973.
(132) Longo, G., and Szleifer, I. (2005) Ligand-receptor interactions in tethered polymer layers. *Langmuir 21*, 11342−11351.
(133) Ahlers, M., Grainger, D. W., Herron, J. N., Lim, K., Ringsdorf, H., and Salesse, C. (1992) Quenching of fluorescein-conjugated lipids by antibodies. Quantitative recognition and binding of lipid-bound haptens in biomembrane models, formation of two-dimensional protein domains and molecular dynamics simulations. *Biophys. J. 63*, 823−838.
(134) Leckband, D. E., Kuhl, T., Wang, H. K., Herron, J., Muller, W., and Ringsdorf, H. (1995) 4−4-20-Anti-fluorescyl IgG Fab' recognition of membrane-bound hapten: direct evidence for the role of protein and interfacial structure. *Biochemistry 34*, 11467−11478.
(135) Cooper, A. D., Balakrishnan, K., and McConnell, H. M. (1981) Mobile haptens in liposomes stimulate serotonin release by rat basophil leukemia-cells in the presence of specific immunoglobulin-E. *J. Biol. Chem. 256*, 9379−9381.
(136) Kimura, K., Arata, Y., Yasuda, T., Kinosita, K., and Nakanishi, M. (1990) Location of membrane-bound hapten with different length spacers. *Immunology 69*, 323−328.
(137) Yamada, K. M., and Geiger, B. (1997) Molecular interactions in cell adhesion complexes. *Curr. Opin. Cell Biol. 9*, 76−85.
(138) Johansson, S., Svineng, G., Wennerberg, K., Armulik, A., and Lohikangas, L. (1997) Fibronectin-integrin interactions. *Front. Biosci. 2*, d126−146.
(139) Yim, E. K. F., Darling, E. M., Kulangara, K., Guilak, F., and Leong, K. W. (2010) Nanotopography-induced changes in focal adhesions, cytoskeletal organization, and mechanical properties of human mesenchymal stem cells. *Biomaterials 31*, 1299−1306.
(140) Xiong, J. P., Stehle, T., Zhang, R. G., Joachimiak, A., Frech, M., Goodman, S. L., and Arnaout, M. A. (2002) Crystal structure of the extracellular segment of integrin alpha V beta 3 in complex with an Arg-Gly-Asp ligand. *Science 296*, 151−155.
(141) Mrksich, M., Dike, L. E., Tien, J., Ingber, D. E., and Whitesides, G. M. (1997) Using microcontact printing to pattern the attachment of mammalian cells to self-assembled monolayers of alkanethiolates on transparent films of gold and silver. *Exp. Cell Res. 235*, 305−313.
(142) Chen, C. S., Mrksich, M., Huang, S., Whitesides, G. M., and Ingber, D. E. (1997) Geometric control of cell life and death. *Science 276*, 1425−1428.
(143) Lehnert, D., Wehrle-Haller, B., David, C., Weiland, U., Ballestrem, C., Imhof, B. A., and Bastmeyer, M. (2004) Cell behaviour on micropatterned substrata: limits of extracellular matrix geometry for spreading and adhesion. *J. Cell Sci. 117*, 41−52.
(144) Lee, S. J., Son, Y., Kim, C. H., and Choi, M. (2007) Fabrication of micro patterned fibronectin for studying adhesion and alignment behavior of human dermal fibroblasts. *Macromol. Res. 15*, 348−356.
(145) Mrksich, M. (2009) Using self-assembled monolayers to model the extracellular matrix. *Acta Biomater. 5*, 832−841.
(146) Grinnell, F., and Feld, M. K. (1982) Fibronectin adsorption on hydrophilic and hydrophobic surfaces detected by antibody binding and analyzed during cell adhesion in serum-containing medium. *J. Biol. Chem. 257*, 4888−4893.
(147) Iwamoto, G. K., Winterton, L. C., Stoker, R. S., Van Wagenen, R. A., Andrade, J. D., and Mosher, D. F. (1985) Fibronectin adsorption detected by interfacial fluorescence. *J. Colloid Interface Sci. 106*, 459−464.
(148) Shi, L., Li, J. R., Shih, Y. P., Lo, S. H., and Liu, G. Y. (2012) Nanogratings of fibronectin provide an effective biochemical cue for regulating focal adhesion and cellular structure. *Nano Res.*, DOI: 10.1007/s12274-012-0242-1.
(149) Gao, P., and Cai, Y. G. (2008) The boundary molecules in a lysozyme pattern exhibit preferential antibody binding. *Langmuir 24*, 10334−10339.
(150) Mogilner, A., and Rubinstein, B. (2005) The physics of filopodial protrusion. *Biophys. J. 89*, 782−795.
(151) Chan, K. T., Cortesio, C. L., and Huttentocher, A. (2007) Integrins in cell migration. *Integrins*, 47−67.
(152) Aratyn-Schaus, Y., Oakes, P. W., Stricker, J., Winter, S. P., and Gardel, M. L. (2010) Preparation of complaint matrices for quantifying cellular contraction. *J. Visualized Exp. 46*, e2173.
(153) Gugutkov, D., Altankov, G., Rodriguez Hernandez, J. C., Monleon Pradas, M., and Salmeron Sanchez, M. (2010) Fibronectin activity on substrates with controlled –OH density. *J. Biomed. Mater. Res., Part A 92*, 322−331.
(154) Bergkvist, M., Carlsson, J., and Oscarsson, S. (2003) Surface-dependent conformations of human plasma fibronectin adsorbed to silica, mica, and hydrophobic surfaces, studied with use of Atomic Force Microscopy. *J. Biomed. Mater. Res., Part A 64A*, 349−356.
(155) Vallieres, K., Chevallier, P., Sarra-Bournett, C., Turgeon, S., and Laroche, G. (2007) AFM Imaging of immobilized fibronectin: Does the surface conjugation scheme affect the protein orientation/conformation? *Langmuir 23*, 9745−9751.
(156) Chen, H. Y., Duncan, I. C., Bozorgchami, H., and Lo, S. H. (2002) Tensin1 and a previously undocumented family member, tensin2, positively regulate cell migration. *Proc. Natl. Acad. Sci. U. S. A. 99*, 733−738.
(157) Haga, H., Nagayama, M., Kawabata, K., Ito, E., Ushiki, T., and Sambongi, T. (2000) Time-lapse viscoelastic imaging of living fibroblasts using force modulation mode in AFM. *J. Electron Microsc. 49*, 473−481.
(158) Hamilton, D. W., Oates, C. J., Hasanzadeh, A., and Mittler, S. (2010) Migration of periodontal ligament fibroblasts on nanometric topographical patterns: Influence of filopodia and focal adhesions on contact guidance. *PLoS One 5*, e15129.
(159) Loesberg, W. A., te Riet, J., van Delft, F. C. M. J. M., Schon, P., Figdor, C. G., Speller, S., van Loon, J. J. W. A., Walboomers, X. F., and Jansen, J. A. (2007) The threshold at which substrate nanogroove dimensions may influence fibroblast alignment and adhesion. *Biomaterials 28*, 3944−3951.
(160) Teixeira, A. I., Abrams, G. A., Murphy, C. J., and Nealey, P. F. (2003) Cell behavior on lithographically defined nanostructured substrates. *J. Vac. Sci. Technol. B 21*, 683−687.
(161) Kim, D. H., Han, K., Gupta, K., Kwon, K. W., Suh, K. Y., and Levchenko, A. (2009) Mechanosensitivity of fibroblast cell shape and movement to anisotropic substratum topography gradients. *Biomaterials 30*, 5433−5444.
(162) Mattila, P. K., and Lappalainen, P. (2008) Filopodia: molecular architecture and cellular functions. *Nat. Rev. Mol. Cell Biol. 9*, 446−454.
(163) Galbraith, C. G., Yamada, K. M., and Galbraith, J. A. (2007) Polymerizing actin fibers position integrins primed to probe for adhesion sites. *Science 315*, 992−995.
(164) Partridge, M. A., and Marcantonio, E. E. (2006) Initiation of attachment and generation of mature focal adhesions by integrin-containing filopodia in cell spreading. *Mol. Biol. Cell 17*, 4237−4248.
(165) Amano, M., Chihara, K., Kimura, K., Fukata, Y., Nakamura, N., Matsuura, Y., and Kaibuchi, K. (1997) Formation of actin stress fibers and focal adhesions enhanced by Rho-kinase. *Science 275*, 1308−1311.
(166) Oakley, C., Jaeger, N. A. F., and Brunette, D. M. (1997) Sensitivity of fibroblasts and their cytoskeletons to substratum topographies: Topographic guidance and topographic compensation by micromachined grooves of different dimensions. *Exp. Cell Res. 234*, 413−424.
(167) Critchley, D. R. (2000) Focal adhesions - the cytoskeletal connection. *Curr. Opin. Cell Biol. 12*, 133−139.
(168) Chen, H. Y., and Lo, S. H. (2003) Regulation of tensin-promoted cell migration by its focal adhesion binding and Src homology domain 2. *Biochem. J. 370*, 1039−1045.
(169) Lo, S. H. (2006) Focal adhesions: What's new inside. *Dev. Biol. 294*, 280−291.
(170) Teixeira, A. I., Abrams, G. A., Bertics, P. J., Murphy, C. J., and Nealey, P. F. (2003) Epithelial contact guidance on well-defined micro- and nanostructured substrates. *J. Cell Sci. 116*, 1881−1892.

(171) Kim, D. H., Seo, C. H., Han, K., Kwon, K. W., Levchenko, A., and Suh, K. Y. (2009) Guided cell migration on microtextured substrates with variable local density and anisotropy. *Adv. Funct. Mater. 19*, 1579−1586.
(172) Defilippi, P., Olivo, C., Venturino, M., Dolce, L., Silengo, L., and Tarone, G. (1999) Actin cytoskeleton organization in response to integrin-mediated adhesion. *Microsc. Res. Techn. 47*, 67−78.
(173) Sastry, S. K., and Burridge, K. (2000) Focal adhesions: A nexus for intracellular signaling and cytoskeletal dynamics. *Exp. Cell Res. 261*, 25−36.
(174) Wozniak, M. A., Modzelewska, K., Kwong, L., and Keely, P. J. (2004) Focal adhesion regulation of cell behavior. *Biochim. Biophys. Acta 1692*, 103−119.
(175) Slater, J. H., and Frey, W. (2008) Nanopatterning of fibronectin and the influence of integrin clustering on endothelial cell spreading and proliferation. *J. Biomed. Mater. Res., Part A 87A*, 176−195.
(176) Pesen, D., and Haviland, D. B. (2009) Modulation of cell adhesion complexes by surface protein patterns. *ACS Appl. Mater. Interfaces 1*, 543−548.
(177) Dalby, M. J., Gadegaard, N., Tare, R., Andar, A., Riehle, M. O., Herzyk, P., Wilkinson, C. D. W., and Oreffo, R. O. C. (2007) The control of human mesenchymal cell differentiation using nanoscale symmetry and disorder. *Nat. Mater. 6*, 997−1003.
(178) Barrias, C. C., Martins, M. C. L., Almeida-Porada, G., Barbosa, M. A., and Granja, P. L. (2009) The correlation between the adsorption of adhesive proteins and cell behaviour on hydroxyl-methyl mixed self-assembled monolayers. *Biomaterials 30*, 307−316.